

Applications of Deep Learning to Ocean Data Inference and Sub-Grid Parameterisation

Thomas Bolton¹, Laure Zanna¹

¹Department of Physics, University of Oxford, UK.

Key Points:

- We successfully use convolutional neural networks to predict unresolved turbulent processes and sub-surface velocities.
- The neural networks generalise to different regions and model configurations.
- Global momentum conservation can be respected without sacrificing accuracy.

Corresponding author: Thomas Bolton, tom.bolton@physics.ox.ac.uk

Abstract

Oceanographic observations are limited by sampling rates, while ocean models are limited by finite resolution and high viscosity and diffusion coefficients. Therefore both data from observations and ocean models lack information at small-scales. Methods are needed to either extract information, extrapolate, or up-scale existing oceanographic datasets, to account for the unresolved physical processes. Here we use machine learning to leverage observations and model data by predicting unresolved turbulent processes and sub-surface flow fields. As a proof-of-concept, we train convolutional neural networks on degraded-data from a high-resolution quasi-geostrophic ocean model. We demonstrate that convolutional neural networks successfully replicate the spatio-temporal variability of the sub-grid eddy momentum forcing, are capable of generalising to a range of dynamical behaviours, and can be forced to respect global momentum conservation. The training data of our convolutional neural networks can be sub-sampled to 10-20% of the original size without a significant increase in accuracy. We also show that the sub-surface flow field can be predicted using only information at the surface, mimicking when only satellite altimetry data is available. Our study indicates that data-driven approaches can be exploited while respecting physical principles, even when data is limited to a particular region or external forcing.

1 Introduction

Satellite observations have produced a wealth of information on the ocean circulation [Morrow *et al.*, 1994; Le Traon and Morrow, 2001; Scott and Wang, 2005; Chelton *et al.*, 2007; Greatbatch *et al.*, 2010b; Abernathey and Marshall, 2013]. However raw satellite altimetry data sub-samples the ocean, and does not measure sub-surface quantities. Temporally measurements at the same location are made twice every orbital cycle, while the spatial sampling depends upon the distance between ground tracks. To improve the sub-sampling rates, measurements from multiple satellites are combined [Le Traon *et al.*, 1998] to produce an optimal estimate.

The process of combining measurements from multiple satellites includes spatio-temporal filtering, which leads to a more ‘smoothed’ view of the dynamical processes at the oceans surface, removing variability due to mesoscale and sub-mesoscale eddies. The filtering can also lead to spurious physical signals, as studied by Arbic *et al.* [2013], which showed that filtering data can lead to exaggerated forward-cascades of energy. The new Surface Water and Ocean Topography (SWOT) mission will have a large swath of 120 km, providing unprecedented detail on the oceans surface. Despite the high spatial sampling rate, measurements may still be limited by the temporal sampling rate of 11 days [Durand *et al.*, 2010].

Similar to satellite observations, Ocean General Circulation Models (OGCM) are useful for studying ocean dynamics. However, high-resolution models are computationally expensive, and the current resolution of models is not high enough to fully resolve the first baroclinic deformation radius at mid-latitudes [Hallberg, 2013]. Also, due to their finite resolution, they require large viscosity and diffusion coefficients in order to remain numerically stable [Jochum *et al.*, 2008]. The combination of finite-resolution and artificially high viscosity, diffuses momentum and smooths out features such as jets and mesoscale eddies [Hewitt *et al.*, 2016; Kjellsson and Zanna, 2017].

Therefore both observations and models are missing the interactions of oceanic turbulence at small-scales, which play an important role in maintaining the large-scale circulation [Greatbatch *et al.*, 2010a,b; Waterman and Jayne, 2010; Waterman *et al.*, 2011; Kang and Curchitser, 2015]; with satellite observations only providing surface information. We thus consider the general problem: given some smoothed view of the oceans surface, what information can be generated on small-scale turbulent interactions and sub-surface quantities. Illuminating unresolved quantities using ‘seen’ quantities would ex-

61 tend the reach of existing datasets, and could potentially improve the representations
62 of unresolved eddies in OGCMs.

63 We tackle this problem with machine learning. Machine learning has grown in pop-
64 ularity in recent years, and has been applied to weather prediction [*McGovern et al.*, 2017;
65 *Esteves et al.*, 2018], climate model parameter sensitivity studies [*Anderson and Lucas*,
66 2018], chaotic dynamical systems forecasting [*Pathak et al.*, 2018a,b; *Vlachas et al.*, 2018],
67 and parameterising unresolved atmospheric processes [*Gentine et al.*, 2018; *Brenowitz*
68 *and Bretherton*, 2018; *Jiang et al.*, 2018; *O’Gorman and Dwyer*, 2018]. The foundational
69 principle of machine learning is extracting information from data. When used to improve
70 our understanding of the earth system, these data-driven methods are an empirical bottom-
71 up approach, whereas the rationalist top-down approach considers physical principles
72 and mechanisms. Here we take the empirical route by exploiting recent developments
73 in machine learning.

74 Using empirical methods to leverage ocean observations is not new. For example,
75 using satellite altimetry data, *Keating et al.* [2012] constructed a stochastic model to ‘super-
76 resolve’ the velocity field and predict the velocity at depth. Similarly, *Keating and Smith*
77 [2015] used a stochastic model to produce a super-resolved sea-surface temperature (SST)
78 field, given a low-resolution observation of SST. With regards to machine learning, *Chap-*
79 *man and Charantonis* [2017] constructed a form of neural network known as a self-organising
80 map to reconstruct sub-surface velocities in the Southern ocean using satellite altime-
81 try data and Argo floats. Other studies have used random forests to predict sub-surface
82 temperature anomalies [*Su et al.*, 2018] and Southern Ocean oxygen content [*Giglio et al.*,
83 2018].

84 In the previous studies that leverage oceanic observations, there is an abundance
85 of coarse-resolution data (satellite altimetry), but limited data on the desired quantities
86 (e.g high-resolution SST or Argo sub-surface velocities); as is the case with OGCMs, where
87 high-resolution data is less readily available due to the computational cost. A similar chal-
88 lenge is when data is only available for particular regions, such as mooring data [*Hogg*,
89 1992] or gliders [*Rudnick et al.*, 2004; *Davis et al.*, 2008]. A machine learning algorithm
90 trained on region-limited data would have to adapt to new regions with different physics;
91 this task is well suited to a deep neural networks, which are known for a strong ability
92 to generalise [*Krizhevsky et al.*, 2012; *LeCun et al.*, 2015; *Goodfellow et al.*, 2016].

93 However, deep neural networks are typically considered a ‘black box’, i.e., they lack
94 simple interpretations. It is therefore difficult to assess whether such data-driven meth-
95 ods respect physical principles (e.g. conservation of energy or momentum). For exam-
96 ple, neural networks have been used to develop Reynolds-averaged turbulence models
97 [*Tracey et al.*, 2015; *Kutz*, 2017], where the studies of *Ling et al.* [2016a,b] in particu-
98 lar show that a neural network can respect Galilean invariance by utilising the invari-
99 ant tensors of *Pope* [1975]. The studies of *Ling et al.* [2016a,b] are important in mov-
100 ing towards data-driven approaches that respect the physical properties of the system.

101 In this paper we focus on a particular machine learning algorithm, namely convo-
102 lutional neural networks, in order to leverage observations and coarse-resolution model
103 data. Our aim is to test whether they can be used to reveal information on unresolved
104 turbulent processes and sub-surface flow fields, and to determine if they are suited to sit-
105 uations where data is limited to a particular region. To move towards these aims, as a
106 proof-of-concept we will address the following questions:

- 107 1. Can convolutional neural networks represent the spatio-temporal variability of the
108 sub-grid eddy momentum forcing.
- 109 2. How sensitive are the neural networks to the physical processes occurring within
110 each region, and how well do they generalise to ocean models in different config-
111 urations.

- 112 3. Is it possible to physically-constrain neural networks to respect global momentum
 113 conservation.
 114 4. Using only information at the surface, can neural networks predict the sub-surface
 115 flow fields.

116 By using data from an idealised high-resolution ocean model, we show that con-
 117 volutional neural networks can represent both the spatial and temporal variability of the
 118 eddy momentum forcing. The region the neural network is trained on, and therefore the
 119 dynamical processes occurring within that region, significantly impact the performance
 120 of the neural network. In particular, training on the most turbulent region produces the
 121 best overall performing neural network. The neural networks successfully generalise to
 122 models with different viscosity coefficients and external wind forcings. Initially momen-
 123 tum is not conserved globally, but the neural networks can be constrained to respect mo-
 124 mentum conservation without a significant reduction in accuracy. A neural network can
 125 accurately predict the sub-surface flow field when there is a strong barotropic compo-
 126 nent to the flow.

127 The paper is organised as follows. The quasi-geostrophic ocean model, the degrad-
 128 ing of model data, and convolutional neural network, are introduced in Section 2. Per-
 129 formance diagnostics of the neural networks, in terms of non-local predictions and gen-
 130 eralising to different model configurations, are presented in Section 3. We explore meth-
 131 ods of physically-constraining the neural networks in Section 5. Section 6 presents a neu-
 132 ral network trained to predict sub-surface flow fields using only information at the sur-
 133 face. We summarise and discuss our results in Section 7.

134 2 Data and Methods

135 2.1 Quasi-Geostrophic Ocean Model

136 We use the PEQUOD model which solves the three-dimensional baroclinic quasi-
 137 geostrophic (QG) potential vorticity equation, with constant wind forcing on a beta plane
 138 [e.g. *Berloff, 2005*]. The model has a bounded-square domain with a flat bottom.

139 The configuration of this model leads to two large-scale circulation gyres separated
 140 latitudinally by a strong meandering zonal jet. The model is configured to represent an
 141 idealised version of current systems such as the Gulf Stream in the North Atlantic or the
 142 Kuroshio Extension in the North Pacific; both these current systems exhibit vigorous
 143 eddies interacting with a strong mean-flow. The time-mean streamfunction, which illus-
 144 trates the double-gyre flow structure, can be seen in Figure 1a of *Mana and Zanna [2014]*.

145 The potential vorticity q is given by

$$q = \nabla^2 q + \beta y + \frac{\partial}{\partial z} \left(\frac{f_0^2}{N^2} \frac{\partial \psi}{\partial z} \right), \quad (1)$$

146 where $f = f_0 + \beta y$ is the planetary vorticity, f_0 is the Coriolis parameter, $\beta =$
 147 df/dy is the Rossby parameter, $\nabla = (\partial/\partial x, \partial/\partial y)$ is the horizontal gradient operator,
 148 $N = \left(-\frac{g}{\rho} \frac{d\rho}{dz}\right)^{\frac{1}{2}}$ is the Brunt-Väisälä frequency, g is gravity, ρ is density, and ψ is the
 149 streamfunction for the non-divergent horizontal velocity $\mathbf{u} = (-\partial\psi/\partial y, \partial\psi/\partial x)$.

150 The model has three layers ($m = 1$ upper, $m = 2$ middle, $m = 3$ upper), with
 151 thicknesses H_m of 250 m, 750 m, 3000 m, respectively. For each layer, the following prog-
 152 nostic equation is solved

$$\frac{\partial q}{\partial t} + (\mathbf{u} \cdot \nabla)q = \mathcal{D} + \mathcal{F}, \quad (2)$$

153 where $\mathcal{D} = \nu \nabla^4 \psi - r \nabla^2 \psi \delta_{m,3}$ is the dissipation, and $\mathcal{F} = (\nabla \times \tau)_z \delta_{m,1} / \rho_0 H_1$ is
 154 the applied wind stress curl forcing, where $\delta_{i,j}$ is the Kronecker delta function. The hor-
 155 izontal resolution of the model is 7.5 km, such that the model is eddy resolving. The first
 156 term in the dissipation is a fourth-order term equivalent to Laplacian viscosity, with vis-
 157 cosity coefficient ν . The second dissipation term parameterises the presence of an Ek-
 158 man layer with bottom drag coefficient r (and therefore only acts on the bottom $m =$
 159 3 layer). The wind stress forcing applied to the upper $m = 1$ layer is given explicitly
 160 by

$$\mathcal{F}(x, y) = \begin{cases} -\tau_0 \frac{0.92\pi}{L\rho_0 H_1} \sin\left(\frac{\pi y}{g(x)}\right) & y \leq g(x), \\ \tau_0 \frac{2\pi}{0.9L\rho_0 H_1} \sin\left(\frac{\pi[2y-g(x)]}{L-g(x)}\right) & y > g(x), \end{cases} \quad (3)$$

161 where $g(x) = L/2 + 0.2(x - L/2)$, $L = 3840$ km is the domain length, and ρ_0 is
 162 the reference density. After the model has been integrated from rest to a statistically steady
 163 state, we save 10 years of model output at daily resolution of the turbulent double-gyre
 164 circulation. For further details on the QG model, see *Mana and Zanna* [2014]; *Zanna*
 165 *et al.* [2017], and for a list of the model parameters see Table 1. We use the data gener-
 166 ated by the ocean model to train various neural networks, but only after degrading the
 167 data, to make it similar to observations or low-resolution model.

168 2.2 Degrading High-Resolution Data

169 We degrade the fields from the high-resolution QG model using a spatial 2D low-
 170 pass filter, in order to produce data that is similar to satellite altimetry or a model with
 171 a large numerical dissipation. From the filtering of the model data, we can then calcu-
 172 late the forcing from unresolved small-scale turbulent processes.

173 At every time slice in the data, we take a high-resolution variable a at a particu-
 174 lar layer, and apply a two-dimensional spatial Gaussian filter. We denote filtered vari-
 175 ables as \bar{a} , and sub-filter variables as the deviation from the filtered variable $a' = a -$
 176 \bar{a} . The value of a function $a(x, y)$, after the Gaussian low-pass filtering operation $G \star$
 177 a at a point (x_0, y_0) , is given by

$$\begin{aligned} \bar{a}(x_0, y_0) &= G \star a = \iint a(x, y) G(x_0, y_0, x, y) dx dy \\ &= \frac{1}{2\pi\sigma^2} \iint a(x, y) e^{-((x-x_0)^2 + (y-y_0)^2)/2\sigma^2} dx dy, \end{aligned} \quad (4)$$

178 where $\sigma = 30$ km is the standard deviation of the Gaussian filter, which deter-
 179 mines the length-scale at which information (below that length-scale) is removed. There-
 180 fore the filter acts to remove information on dynamical processes at spatial scales smaller
 181 than 30 km.

182 Using the low-pass filter defined in Equation 4, we can now express the effects of
 183 the unresolved (sub-filter) variables onto the resolved (filtered) variables. Ignoring ver-
 184 tical effects and planetary vorticity, the horizontal momentum equation is given by

$$\frac{\partial \mathbf{u}}{\partial t} + (\mathbf{u} \cdot \nabla) \mathbf{u} = \mathbf{F} + \mathbf{D}, \quad (5)$$

185 where \mathbf{F} and \mathbf{D} are the momentum forcing and dissipation, respectively. Apply-
 186 ing a low-pass filter to Equation 5, and then adding $(\bar{\mathbf{u}} \cdot \nabla) \bar{\mathbf{u}}$ to both sides of the equa-
 187 tion, leads to

$$\frac{\partial \bar{\mathbf{u}}}{\partial t} + (\bar{\mathbf{u}} \cdot \nabla) \bar{\mathbf{u}} = \bar{\mathbf{F}} + \bar{\mathbf{D}} + [(\bar{\mathbf{u}} \cdot \nabla) \bar{\mathbf{u}} - \overline{(\mathbf{u} \cdot \nabla) \mathbf{u}}], \quad (6)$$

$$\frac{\partial \bar{\mathbf{u}}}{\partial t} + (\bar{\mathbf{u}} \cdot \nabla) \bar{\mathbf{u}} = \bar{\mathbf{F}} + \bar{\mathbf{D}} + \mathbf{S}, \quad (7)$$

$$\text{where } \mathbf{S} = \underbrace{(\bar{\mathbf{u}} \cdot \nabla) \bar{\mathbf{u}} - \overline{(\mathbf{u} \cdot \nabla) \mathbf{u}}}_{\text{Sub-filter eddy momentum forcing.}} \quad (8)$$

188 The low-pass filtering operation results in an additional forcing term in Equation 7
 189 for the filtered momentum; the additional momentum forcing \mathbf{S} is given by Equation 8,
 190 the divergence of a Reynolds stress. The vector $\mathbf{S} = (S_x, S_y)$ represents the effects of
 191 the sub-filter momentum field on the filtered momentum field, i.e., the interaction be-
 192 tween small-scale eddies and the large-scale flow. As the sub-filter eddy forcing \mathbf{S} depends
 193 on the sub-filter variables, it requires a physical parameterisation or closure.

194 2.3 Predictive Algorithm: Convolutional Neural Networks

195 Convolutional Neural Networks (CNNs) have proven successful in many areas of
 196 computer vision [Krizhevsky et al., 2012; Simonyan and Zisserman, 2014; Dong et al.,
 197 2016], where the primary objective is to extract information from an image, in order to
 198 perform a particular task. CNNs work by applying successive layers of convolutions (a
 199 form of spatial filtering) to the input; the complexity of the extracted information in-
 200 creases with the number of convolution layers. The powerful property of CNNs is that
 201 the filters of each convolution are learnt as part of the training process - they are not spec-
 202 ified a priori. Therefore CNNs learn to extract the most ‘useful’ information from the
 203 input variable, given training on a particular dataset.

204 We chose to use CNNs, as opposed to a deep neural network of multiple fully-connected
 205 layers, due to their superior performance in computer vision tasks where the inputs have
 206 a two dimensional structure [Krizhevsky et al., 2012]. We wanted a machine learning al-
 207 gorithm that could exploit the two dimensional lateral structure of turbulent fluids. Spa-
 208 tial filtering of the equations of motion of turbulent fluids is not new, and is used in Large
 209 Eddy Simulation (LES) [Moeng, 1984; Sagaut, 2006]. Therefore, the learnt-filtering op-
 210 erations of a CNN appeared to be a natural choice of data-driven algorithm to apply to
 211 geophysical flows.

212 The training process involves the minimisation of an appropriately defined loss func-
 213 tion, which measures the difference between the output of the CNN, and the desired tar-
 214 gets. If the optimisation procedure was successful, such that the loss function on pre-
 215 viously unseen data converges, the CNN will have learnt to extract the most important
 216 information from the input. The CNN then uses the information to predict continuous
 217 values. The CNN constructs the final prediction through a linear regression layer, which
 218 regresses the desired output onto the final feature maps (feature maps are the interme-
 219 diate results of each convolution layer).

220 Here we use CNNs to represent the sub-filter eddy momentum forcing. The input
 221 is the filtered-streamfunction $\bar{\psi}$ of the upper vertical layer, which represents our resolved
 222 variable that the neural networks will extract information from. The output variables
 223 are the zonal S_x and meridional S_y components of the sub-filter momentum forcing \mathbf{S} ,
 224 defined by Equation 8. An example input and output is shown in Figure 1. Separate CNNs
 225 are trained for each component of the sub-filter momentum forcing S_x and S_y . We only
 226 consider data from the upper-layer of the model; this is because the flow is surface-intensified,
 227 and we are assuming that our filtered quantities are similar to satellite altimetry data,
 228 which only provide information at the surface.

229 In addition to testing whether it is possible to train a neural network to predict
 230 S_x and S_y , from $\bar{\psi}$, we explore how a neural network trained on one region performs on
 231 another previously unseen region, i.e. how important local vs non-local information is
 232 for different regions. We therefore construct three different datasets from the QG model
 233 data, one for each region being studied. We choose regions which differ most in their dy-
 234 namical behaviour, and are shown in Figure 1a: Region 1 is near the jet-separation point
 235 of the western boundary, where there is a strong, inertial zonal jet. Region 2 is near the
 236 eastern boundary downstream of the jet extension, where the dynamics are more wave-
 237 like in nature. Region 3 is in the centre of the southern gyre, which is energetically less
 238 active than regions 1 and 2.

239 Data from the three regions are split temporally into training and validation datasets.
 240 The 10-years of daily data (3650 days) are split into the first ~ 9 years (3300 days) to
 241 train the neural networks, and the final year (350 days) is set aside for validation. To
 242 reduce the computational cost, and the number of parameters of each CNN, we split each
 243 region spatially from the initial 160×160 grid points, to sixteen 40×40 grid point sub-
 244 regions, as depicted in Figure 1c. Reducing the input and output size of the neural net-
 245 work from 160×160 to 40×40 significantly decreases the number of trainable weights,
 246 and therefore the computational cost (we attempted to make predictions for the full 160×160
 247 of each training region, but this led to a neural network with over 250,000,000 param-
 248 eters, which was computationally impractical).

249 Making predictions for a 40×40 area instead of a 160×160 area also increases the
 250 amount of training and validation data by a factor of sixteen, from 3300 and 350 sam-
 251 ples, to 52800 and 5600 respectively, where a sample is defined as a single input-output
 252 pair of the neural network. We therefore have 52800 spatial maps (size 40×40 grid points)
 253 of input-output pairs to train the neural networks, and 5600 spatial maps of input-output
 254 pairs set aside for validation.

255 We train CNNs to separately predict S_x and S_y , using data from three different
 256 regions of the model; this gives a total of 6 neural networks. Each neural network is de-
 257 noted by $f_i(\bar{\psi}, \mathbf{w}_R)$, where $i = (x, y)$ refers to the component of \mathbf{S} being predicted, \mathbf{w}_R
 258 are the trained weights of the neural network, and $R = 1, 2, 3$ refers to the region on
 259 which the neural network has been trained. For example, the neural network trained on
 260 region 2 to predict the meridional component S_y is denoted by $f_y(\bar{\psi}, \mathbf{w}_2)$.

To distinguish predictions from the true values, we label neural network predictions
 as $\tilde{S}_x = f_x(\bar{\psi}, \mathbf{w}_R)$, and $\tilde{S}_y = f_y(\bar{\psi}, \mathbf{w}_R)$, while the true values of the sub-filter mo-
 mentum forcing remain as S_x, S_y . We use the mean-squared error as the loss function,

$$L = \sum (S_x - \tilde{S}_x)^2, \text{ or } \sum (S_y - \tilde{S}_y)^2, \quad (9)$$

261 which quantifies the difference between the neural network predictions and the truth,
 262 and where the summation is over all samples. The neural networks are trained (i.e. opti-
 263 mised) using a form of stochastic gradient descent, namely the Adam optimisation al-
 264 gorithm [Kingma and Ba, 2014], which minimises the loss function L defined in Equa-
 265 tion 9. The training of each neural network $f_i(\bar{\psi}, \mathbf{w}_R)$, iteratively adjusts the values of
 266 the weights \mathbf{w}_R , such that the loss function in Equation 9 is minimised. Therefore each
 267 neural network has a different set of weights \mathbf{w}_R ; it is these weights which determine how
 268 each neural network extracts information and makes predictions.

269 The architecture used for each $f_i(\bar{\psi}, \mathbf{w}_R)$ contains three convolution layers, a max
 270 pooling layer, and a final fully-connected layer (Figure 1). The max pooling layer reduces
 271 the dimensionality of the previous layer, by selecting the maximum value within a 2×2
 272 grid point area - max pooling is effective when there is significant correlation between
 273 points in the feature maps. To give the neural networks the ability to learn non-linear
 274 functions, activation functions are added between layers. Here we use the scaled expo-
 275 nential linear unit (SELU) [Klambauer et al., 2017]. SELU activation functions scale the

276 data towards zero mean and unit variance, removing the need for batch normalisation
 277 - batch normalisation enforces zero mean and unit variance at each stage of the network,
 278 but requires additional training.

279 The specific architecture was constructed by adjusting all parameters and observ-
 280 ing which configuration most effectively minimises the loss function on the validation data.
 281 See Table 1 for more details of the architecture and training procedure. The total num-
 282 ber of parameters of each neural network is 325,728.

283 We train and implement each neural network using Keras [Chollet et al., 2015], with
 284 the Tensorflow backend [Abadi et al., 2016]. Before training, all datasets are separately
 285 normalised to zero mean and unit variance. Each CNN is trained for 200 epochs (1 epoch
 286 = 1 full pass of all the training data through the optimisation algorithm), taking approx-
 287 imately 10 CPU hours, after which there is negligible change in the loss function of the
 288 validation data.

289 Once all six neural networks are trained, we make the predictions \tilde{S}_x and \tilde{S}_y us-
 290 ing the filtered-stream function $\bar{\psi}$ from the validation dataset, i.e., the final year of with-
 291 held data. We make predictions for the full-domain to determine how each neural net-
 292 work generalises to unseen, dynamically-distinct, regions. As the input and output size
 293 of each neural network is 40×40 grid points, we tile together predictions for the full do-
 294 main of size 512×512 ; the tiling leads to errors at the boundaries of each tile, where dis-
 295 continuities can emerge. To reduce the tiling error, we make predictions using overlap-
 296 ping tiles, and then average the results at each grid point.

297 In order to make predictions of the sub-surface flow field, using only information
 298 at the surface, we train a new neural networks. The new neural network has an iden-
 299 tical architecture to those discussed previously, and is trained to predict the middle-layer
 300 streamfunction using the upper-layer streamfunction as the input; this neural network
 301 is described in more detail in Section 6.

302 **3 Neural Network Sensitivity and Generalisation**

303 **3.1 Non-Local Predictions**

304 The filtered streamfunction represents for example observational measurements from
 305 satellite altimetry or coarse-resolution model data. The sub-filter eddy momentum forc-
 306 ing represents unresolved turbulent processes. Our goal is to replicate the complex spatio-
 307 temporal variability of S_x and S_y using neural networks $f_i(\bar{\psi}, \mathbf{w}_R)$. However observa-
 308 tional data such as moorings [Hogg, 1992] or gliders [Rudnick et al., 2004; Davis et al.,
 309 2008], may only be available for a particular region; we therefore only train the neural
 310 networks using data from specific regions of the full domain, as described in Section 2.3.
 311 Our aims are to both successfully train the neural networks, and to study how they gen-
 312 eralise to previously un-seen regions.

313 We study the spatio-temporal variability of S_x and \tilde{S}_x , by examining snapshots,
 314 the time-mean, and the standard deviation, shown in Figure 2. Diagnostics are calcu-
 315 lated over the full 512×512 domain, using the final year of withheld data. Both the spa-
 316 tial and temporal variability of the true S_x are dominated by the jet dynamics (Figure 2a, e, and i).
 317 In particular, strong meanders which extend eastward from the western boundary are
 318 visible. The amplitude of the spatio-temporal variability of S_x ($1.4 \times 10^{-6} \text{ms}^{-2}$) is of sim-
 319 ilar magnitude to the time-mean ($1.5 \times 10^{-6} \text{ms}^{-2}$).

320 All neural networks trained on three different regions, shown in Figure 1a and de-
 321 scribed in Section 2.3, successfully reproduce the spatial patterns of the true S_x , as shown
 322 by snapshots of the predictions \tilde{S}_x (Figure 2b, c, and d). Their magnitudes however vary
 323 significantly. The predictions of $f_x(\bar{\psi}, \mathbf{w}_1)$, trained on data from the western boundary,

324 are almost identical to the true S_x , and successfully reproduces the correct amplitude
 325 and variability (Figure 2b, f, j). The neural network $f_x(\bar{\psi}, \mathbf{w}_2)$, trained on data from the
 326 eastern boundary, underestimates the magnitude of the true S_x by approximately 50%,
 327 despite reproducing the correct spatial patterns. The predictions of $f_x(\bar{\psi}, \mathbf{w}_3)$, trained
 328 on the southern gyre, underestimates the true S_x by an order of magnitude (Figure 2d,
 329 h, l).

330 As the variability of S_x is dominated by the jet, it is difficult to assess the accu-
 331 racy of the neural network predictions \tilde{S}_x in quiescent regions such as the eastern bound-
 332 ary or within the gyres. We therefore calculate the Pearson correlation, a dimensionless
 333 quantity, between the true S_x and the predictions \tilde{S}_x . The predictions of $f_x(\bar{\psi}, \mathbf{w}_1)$ and
 334 $f_x(\bar{\psi}, \mathbf{w}_2)$ are highly correlated with the truth ($r > 0.9$) within the jet, but tend towards
 335 zero or negative correlation near the eastern boundary (Figure 2m and 2n). The predic-
 336 tions of $f_x(\bar{\psi}, \mathbf{w}_3)$ have a more consistent positive correlation across the gyres and other
 337 more quiescent regions, (Figure 2o).

338 We observe similar results for the spatial and temporal variability of S_y , shown in
 339 Figure 3: the variability within the jet dominates, with an amplitude ($1 \times 10^{-6} \text{ms}^{-2}$)
 340 similar to S_x . The meandering of the jet again produces complex spatial patterns in S_y ,
 341 which when averaged in time, produce a distinct sign change moving across the jet lat-
 342 itudinally. For the predictions \tilde{S}_y , the neural network trained on the western boundary,
 343 $f_y(\bar{\psi}, \mathbf{w}_1)$, most effectively reproduces the true S_y . However, the time-mean of $f_y(\bar{\psi}, \mathbf{w}_1)$
 344 (Figure 3f) has a positive bias everywhere in the domain, whereas the time-means of $f_y(\bar{\psi}, \mathbf{w}_2)$
 345 and $f_y(\bar{\psi}, \mathbf{w}_3)$ (Figure 3g and 3h respectively) do not.

346 The correlations between S_y and \tilde{S}_y are similar to the zonal component: $f_y(\bar{\psi}, \mathbf{w}_1)$
 347 and $f_y(\bar{\psi}, \mathbf{w}_2)$ are highly correlated ($r > 0.8$) within the jet, but not in the gyres. Where
 348 as $f_y(\bar{\psi}, \mathbf{w}_3)$ has a consistently positive correlation across the full domain, despite fail-
 349 ing to reproduce the amplitude within the jet. In fact, the correlation of $f_y(\bar{\psi}, \mathbf{w}_3)$ within
 350 the jet (Figure 3o) is negative ($r \approx -0.3$). The negative correlation implies that the
 351 dynamical processes occurring within region 3, the southern gyre, have an opposite ef-
 352 fect to the eddy momentum forcing occurring within region 1. The opposing effects of
 353 eddies could be an example of regional variation in eddy forcing, as in *Waterman and*
 354 *Jayne* [2010], who found that whether eddies were driving the large-scale flow or not,
 355 depended critically on along-stream position.

356 Across all neural networks, the correlation decreases at the eastern boundary, which
 357 is partly caused by the sub-filter momentum forcing being orders of magnitude lower than
 358 elsewhere in the domain. The low magnitude of S_x and S_y is due to the wave-like be-
 359 haviour of the flow having a larger spatial-scale. The larger spatial-scale at the eastern
 360 boundary leads to little variability at small scales, reducing the eddy momentum forc-
 361 ing to almost zero, and therefore causing the performance of neural networks to deter-
 362 iorate.

363 Overall, we see that training neural networks on the western boundary is most suc-
 364 cessful when generalising to other areas of the domain (in terms of correlations and re-
 365 producing the variability). Training on the eastern boundary produced good correlations
 366 in the western boundary, but underestimated the magnitude of the eddy forcing by ap-
 367 proximately 50%. Training on the southern gyre did not correlate well within the west-
 368 ern boundary, and underestimated the truth by an order of magnitude.

369 Hence to successfully reproduce the correct amplitude and variability across the
 370 domain, the training data must contain a diverse range of scale interactions, which here
 371 corresponds to training on the most turbulent region. However, training on the turbu-
 372 lent regions can lead to significant net biases in the predictions, as seen in Figure 3f. How
 373 to correct for such biases will be discussed in Section 5.

374

3.2 Generalising to Different Reynolds Numbers

375

376

377

378

379

380

381

382

383

In Section 3.1, we investigated how neural networks trained on different regions of the domain generalise to other previously unseen regions. We now test how the neural networks generalise to different regimes, in particular different Reynolds number. In Section 3.1, we found that the neural networks trained on region 1, the western boundary, successfully generalised to different regions; we therefore apply $f_x(\bar{\psi}, \mathbf{w}_1)$ to new model data with different wind stress amplitudes and viscosity coefficients to test its performance. We use models with higher and lower wind forcings, to test regimes which are both more and less turbulent than the original model, which had a wind stress amplitude of $\tau_0 = 0.8 \text{ Nm}^{-2}$ and viscosity $\nu = 75 \text{ m}^2\text{s}^{-2}$.

384

385

386

387

388

We use the low-pass on filter the upper-layer streamfunction from each different model run, with the following: $\nu = 200 \text{ m}^2\text{s}^{-2}$, and $\tau_0 = 0.3, 0.6,$ and 0.9 Nm^{-2} , and then apply the already-trained neural network $f_x(\bar{\psi}, \mathbf{w}_1)$ to generate predictions \tilde{S}_x . The standard deviation of the true S_x , the standard deviation of the $f_x(\bar{\psi}, \mathbf{w}_1)$ predictions \tilde{S}_x , and the correlation between them, are shown in Figure 4.

389

390

391

392

393

394

395

396

397

The neural network $f_x(\bar{\psi}, \mathbf{w}_1)$ reproduces the variability within the jet almost exactly, across all runs, as can be seen by comparing the standard deviations in the first and second columns, which represent the standard deviation of the true S_x and predicted \tilde{S}_x respectively. The correlation within the jet remains high ($r > 0.9$) in all runs, including the model with an increased wind forcing ($\tau_0 = 0.9 \text{ Nm}^{-2}$) in Figure 4o. The correlations weaken at the eastern boundary for the lowest wind forcing ($\tau_0 = 0.3 \text{ Nm}^{-2}$), shown in Figure 4f; this may be caused by an increase in the wave-like behaviour at the eastern boundary, which is not well captured by the neural networks. In general, the higher the Reynolds number, the better the correlations, i.e., more dark red areas of $r > 0.8$.

398

399

400

The mean biases of the predictions of the new models are similar in magnitude to the biases of the original model configuration. These biases showed no relationship with the Reynolds number, and are therefore not discussed further.

401

4 Sensitivity of Neural Networks to Under-Sampling

402

403

404

405

406

407

408

409

410

411

We have so far trained the neural networks with densely sampled data, i.e., we have data at each grid point for both the input and output variables. However, most observational datasets are spatially sparse, e.g. Argo floats [Roemmich *et al.*, 2009]. We therefore explore the impact of under-sampling with a new collection of neural networks trained on region 1 to predict S_x , but with the training data sub-sampled. At each time-slice of the training data, we randomly sample (without replacement) N points of the 40×40 input variables, $\bar{\psi}$, and output variables S_x . Using these N randomly sampled values, we use a cubic interpolation to reconstruct the full 40×40 grid point input and output (with a nearest-neighbour interpolation for grid points that fall outside the convex hull of the cubic interpolation).

412

413

414

415

416

417

418

These reconstructed time-slices from sub-sampled data are used to train a new set of neural networks. We vary the number of points N sub-sampled from $> 90\%$ to $< 5\%$ of the original 1600 points of the input and output variables. We have a neural network for each value of N , the sub-sampling rate. Using the neural networks trained on under-sampled data, we calculate the root-mean square error (RMSE) on the final year of validation data over the entire domain. The validation data is not sub-sampled, providing a stronger and more accurate test of the neural networks performance.

419

420

421

422

The RMSE is shown as a function of percentage of points sampled (Figure 7c). We find that the RMSE increases significantly only when the percentage of spatial points sampled drops below 10% (the error doubles at a sub-sampling rate of 4.7%). Note that the RMSE is not a monotonic function of percentage of points sampled due to the stochas-

423 tic nature of the training procedure and the use of a non-linear interpolation. The spa-
 424 tial map of RMSE of the neural network trained with 18.75% sub-sampled data (Fig-
 425 ure 7b) shows minimal changes relative to the neural network trained on the original (un-
 426 altered) training data (Figure 7a). The result further suggests that the use of sparse in-
 427 terpolated observations can be successfully used to accurately train and predict the eddy
 428 momentum forcing as shown in Sections 3.1 and 3.2.

429 We also tested an alternative method of under-sampling, where the 40×40 input
 430 and output grid of the neural network is spaced out over the entire domain. In other words,
 431 we sub-sample the input and output variables of the original 512×512 grid to a regularly
 432 spaced 40×40 grid. However, training a convolutional neural network with this method-
 433 ology did not work and led to severe overfitting (i.e. increasing validation loss during train-
 434 ing). The neural networks presented in Section 2 learn to take first and second order deriva-
 435 tives of the input streamfunction (see GitHub repository), which correspond to the ve-
 436 locities and velocity shears. Both velocities and velocity shears are important features
 437 to provide for accurate predictions of the eddy momentum forcing. By severely sub-sampling
 438 the input streamfunction, the local information relevant to estimate velocities and ve-
 439 locity shears is lost.

440 5 Physically-Constrained Neural Networks

441 We proceed to examine the net input of momentum from the neural network pre-
 442 dictions \tilde{S}_x and \tilde{S}_y , which should vanish. If neural networks are used to leverage the use
 443 of observational datasets and coarse-resolution models, then spurious sources of momen-
 444 tum would violate physical conservation laws. We therefore need to constrain the neu-
 445 ral networks to respect the physical properties of the system. Here we diagnose the mo-
 446 mentum biases of the neural networks $f_i(\bar{\psi}, \mathbf{w}_R)$, and then explore different methods of
 447 imposing conservation of momentum globally.

448 5.1 Momentum Biases

449 Each sub-region (including those used to train the neural networks) may have a
 450 non-zero spatially-integrated momentum tendency. However, globally, the true sub-filter
 451 momentum forcing \mathbf{S} should re-distribute momentum, and not act as a source or sink,
 452 i.e. $\iint \mathbf{S} dx dy = 0$. We therefore need the neural networks to not introduce spurious
 453 sources of momentum, to respect the physical properties of the system. By training each
 454 neural network on a sub-region, we expect to have imperfect momentum conservation,
 455 which will depend upon the particular dynamical processes within each region. For ex-
 456 ample, if eddies within a particular region are driving the mean-flow, then we would ex-
 457 pect a positive source of momentum locally - a neural network trained on such a region
 458 would likely generalise the (local) input of momentum to the rest of the domain. A net
 459 source or sink of momentum will manifest as a non-zero bias after spatial averaging.

460 At a single point in space, the time series of the predictions \tilde{S}_x and \tilde{S}_y show that
 461 the neural networks trained on regions 1 and 2 track the true S_x and S_y closely (Fig-
 462 ure 5a and 5b), reproducing a significant proportion ($> 80\%$) of the variance. However,
 463 if at each time-step we spatially average the neural network predictions \tilde{S}_x and \tilde{S}_y (Fig-
 464 ure 5c and 5d respectively) over the full domain, we observe significant non-zero biases.

465 Consider the zonal component of the eddy momentum forcing in Figure 5c: $f_x(\bar{\psi}, \mathbf{w}_1)$
 466 has a net positive bias, implying a global positive increase of zonal momentum at all times,
 467 while both $f_x(\bar{\psi}, \mathbf{w}_2)$ and $f_x(\bar{\psi}, \mathbf{w}_3)$ have negative biases, indicating a net decrease in
 468 zonal momentum. We can estimate the magnitude of the resulting change in zonal ve-
 469 locity from these net biases, over a period of a year, by assuming $\Delta u = \langle \tilde{S}_x \rangle \Delta t$, where
 470 $\langle \rangle$ denotes the spatial average over the full domain. For $f_x(\bar{\psi}, \mathbf{w}_1)$, $f_x(\bar{\psi}, \mathbf{w}_2)$, and $f_x(\bar{\psi}, \mathbf{w}_3)$,
 471 we obtain values of $\langle \tilde{S}_x \rangle = 0.03, 0.02,$ and 0.0008 (10^{-6}ms^{-2}) respectively; this leads

472 to zonal velocity changes of $\Delta u = 0.95, 0.63, \text{ and } 0.025 \text{ (ms}^{-1}\text{)}$. These changes are of
 473 similar magnitude to the time-mean zonal flow, which peaks at approximately 0.9 ms^{-1}
 474 within the jet core.

475 There are also significant biases in the predictions of the meridional component \tilde{S}_y ,
 476 shown in Figure 5d. The positive bias of $f_y(\bar{\psi}, \mathbf{w}_1)$ is visible in the time-mean \tilde{S}_y shown
 477 in Figure 3f. We can again estimate the change in meridional velocities by assuming $\Delta v =$
 478 $\langle \tilde{S}_y \rangle \Delta t$. Using values of $\langle \tilde{S}_y \rangle = 0.02, -0.01, \text{ and } 0.002 \text{ (} 10^{-6} \text{ms}^{-2}\text{)}$ for $f_y(\bar{\psi}, \mathbf{w}_1), f_y(\bar{\psi}, \mathbf{w}_2),$
 479 and $f_y(\bar{\psi}, \mathbf{w}_3)$ respectively, leads to the following changes: $\Delta v = 0.63, -0.31, \text{ and } 0.06 \text{ (ms}^{-1}\text{)}$.
 480 Some of these changes are the same magnitude as the time-mean meridional flow.

481 5.2 Towards Momentum-Conserving Neural Networks

482 The predictions of neural networks $f_x(\bar{\psi}, \mathbf{w}_1)$ and $f_y(\bar{\psi}, \mathbf{w}_1)$, described in Section 3.1,
 483 correctly reproduce the correct amplitude and variability of the true eddy momentum
 484 forcing S_x and S_y , as seen in Figures 2 and 3. However, training on region 1 also pro-
 485 duced some of the largest non-zero biases in \tilde{S}_x and \tilde{S}_y after spatial averaging at each
 486 time step. We therefore test whether we can reduce the biases when training on region
 487 1, while preserving the accuracy of predictions from the neural network. We trial three
 488 approaches (A, B, and C) to reduce the biases identified in Figure 5c and 5d.

- 489 (A) Architecture Alteration: Train neural networks on region 1, but with the final fully-
 490 connected layer modified such that the spatial mean is removed from the final out-
 491 put. The neural networks will therefore be trained to reproduce the sub-filter mo-
 492 mentum forcing, but with momentum conservation intrinsically embedded. I.e. same
 493 training data, but altered architecture. The motivation behind this approach is
 494 that if the local source of momentum within the 40×40 output grid is zero, then
 495 this may reduce the global net source of momentum.
- 496 (B) Pre-processing of input: Train on region 1 with the original architecture described
 497 in Table 1 but with the spatial-mean removed at each snapshot within the train-
 498 ing data. I.e. enforce momentum conservation in the training data, but make no
 499 changes to the architecture. If the local source of momentum of each 40×40 out-
 500 put grid is zero within the training data, then the neural network may move to-
 501 wards local momentum conservation during training. Though this does not guar-
 502 antee that subsequent predictions will have zero local bias.
- 503 (C) Post-processing of output: train on region 1, and enforce global momentum con-
 504 servation after the predictions have been made. I.e. no changes to training data
 505 or architecture, but with additional processing of the full-domain predictions \tilde{S}_x and \tilde{S}_y .

506 The associated neural networks of each approach are labelled as $f_i(\bar{\psi}, \mathbf{w}_1^A), f_i(\bar{\psi}, \mathbf{w}_1^B),$
 507 and $f_i(\bar{\psi}, \mathbf{w}_1^C)$ respectively, where $i = (x, y)$ denotes either the zonal S_x or meridional
 508 S_y component being predicted.

509 All neural networks are optimised using the same training parameters given in Ta-
 510 ble 1. Approach A, which alters the architecture, and approach B, which alters the train-
 511 ing data, are enforcing momentum conservation not just globally, but within the 40×40
 512 sub-region being predicted. This local conservation is useful for enforcing global conser-
 513 vation. However local conservation may not be desirable if there's convergence of eddy
 514 momentum fluxes in a particular region, which can impact the large-scale flow, e.g. if
 515 eddies are fluxing momentum into the jet at a particular along-stream position, enforc-
 516 ing local conservation in a neural network may lead to missing these effects. Therefore
 517 caution must be taken with restricting architectures in this way.

518 We now explore the performance of the newly constrained neural networks and the
 519 net momentum input relative to that of the original neural networks trained on region

520 1: $f_x(\bar{\psi}, \mathbf{w}_1)$ and $f_y(\bar{\psi}, \mathbf{w}_1)$. The spatial-averages of neural networks based on approaches
521 A, B, and C are shown in Figure 6, with the same scale axes as in Figure 5.

522 Approach B has significant biases of approximately -0.01 and -0.015 (10^{-6}ms^{-2})
523 in the zonal and meridional components respectively; the optimisation procedure aims
524 to reproduce the *variability* in the training data, and not spatial-means, therefore pre-
525 processing the training data does not remove the biases. Compared to the original neu-
526 ral networks trained on region 1, the biases of approaches A and C are 3 to 5 orders of
527 magnitude lower, in both the zonal and meridional components. The post-processing ap-
528 proach is exactly zero by construction, while the altered-architecture approach A is not
529 exactly zero due to the overlapping-tiling procedure. The biases of $f_x(\bar{\psi}, \mathbf{w}_1^A)$ and $f_y(\bar{\psi}, \mathbf{w}_1^A)$
530 are approximately -0.002 and -0.0005 (10^{-6}ms^{-2}) which, over the course of a year, would
531 lead to velocity changes of $\Delta u = -0.06$ and $\Delta v = -0.01$ (ms^{-1}) respectively - now an
532 order of magnitude smaller than the time-mean flow.

533 The correlation maps of all momentum-conserving approaches (not shown) change
534 little from the original correlation maps of $f_x(\bar{\psi}, \mathbf{w}_1)$ and $f_y(\bar{\psi}, \mathbf{w}_1)$, shown in Figure 2m and 3m
535 respectively. All approaches reproduce the correct spatial patterns of the true S_y and
536 S_y (e.g., Figure 6 for standard deviations). However, approaches A and B underestimate
537 the amplitude of S_x and S_y by approximately 20-30%, whereas there is a little difference
538 between approach C and the truth ($< 10\%$).

539 In summary, approach C of post-processing successfully enforces momentum con-
540 servation, without sacrificing accuracy in the predictions of the eddy momentum momen-
541 tum forcing. Approach B, altering the training data, was not efficacious at reducing the
542 net biases. The physically-constrained architecture of approach A successfully reduced
543 the net bias, but at the expense of 20-30% accuracy. Though further altering of the ar-
544 chitecture (e.g. increasing number of convolution layers and filters) or training proce-
545 dure (decreasing the learning rate, with increased number of training epochs) could re-
546 duce this drop in accuracy by countering the restriction placed on the architecture.

547 6 Predicting Sub-Surface Flow

548 We have shown that neural networks, by using the filtered-streamfunction as the
549 input variable, can provide information on unresolved turbulent processes, namely the
550 sub-filter momentum forcing. We have assumed that the filtered-streamfunction repre-
551 sents some limited set of observations, or data from a coarse-resolution ocean model. How-
552 ever, coarse-resolution ocean models still produce data for below the surface, whereas
553 satellite observations do not. Here we address the issue of inferring sub-surface informa-
554 tion solely from surface fields. Our approach is conceptually similar to *Chapman and Cha-*
555 *rantonis* [2017], which used a form of neural network called a self-organising map to re-
556 construct sub-surface velocities in the Southern ocean, using satellite altimetry and Argo
557 float data. Using the QG model data described in Section 2.1, we test whether a neu-
558 ral network can predict the middle-layer streamfunction, using only the surface filtered-
559 streamfunction.

560 We train a new neural network $\tilde{\psi}_2 = f(\bar{\psi}_1, \mathbf{W})$ (which has the same architecture
561 as before, but with a different output and weights) to minimise the mean-squared error
562 loss function $L \propto (\psi_2 - \tilde{\psi}_2)^2$, where $\bar{\psi}_1$ is the filtered-streamfunction of the upper-layer,
563 ψ_2 is the true streamfunction of the middle-layer, and $\tilde{\psi}_2$ is the neural network predic-
564 tions. Again, to assess the ability to generalise to unseen regions, we only train the neu-
565 ral network on the western boundary (training region 1). Diagnostics of the true ψ_2 and
566 predictions $\tilde{\psi}_2$, including the correlation between them, are shown in Figure 8a-e. The
567 neural network accurately reproduces the middle-layer time-mean and standard devia-
568 tion of the streamfunction within the jet region. The neural network accurately repro-
569 duces the correct amplitude of the true ψ_2 within the jet, but underestimates the am-

570 plitude by $\approx 50\%$ within the gyres. Independent of the amplitude, the predictions $\tilde{\psi}_2$ are
 571 highly correlated ($r > 0.8$) almost everywhere in the domain with the true ψ_2 .

572 The decrease in accuracy in the gyres is likely due to only training within the west-
 573 ern boundary, where the streamfunctions of the upper- and middle-layers are more tightly
 574 coupled due to the strong barotropic nature of the flow. Within the gyres, the barotropic
 575 component is not as dominant - this could cause the neural networks to underestimate
 576 the amplitude away from the jet. Alternatively the adjustment time scales of the upper-
 577 and middle-layers are not the same, which perhaps requires more training data in order
 578 to capture interactions over longer time scales.

579 We take the approach one step further, by predicting the bottom-layer streamfunc-
 580 tion, using the same neural network and its weights $f(\bar{\psi}_1, \mathbf{W})$, but now using the pre-
 581 dictions of the middle-layer streamfunction as the input, i.e., $\tilde{\psi}_3 = f(\tilde{\psi}_2, \mathbf{W})$. We test
 582 whether a neural network trained to predict the middle-layer streamfunction can pro-
 583 vide any information on the bottom-layer streamfunction (without re-training), by in-
 584 putting the middle-layer streamfunction as an input. Mathematically, this is written as
 585 $\tilde{\psi}_3 = f(f(\bar{\psi}_1, \mathbf{W}), \mathbf{W})$.

586 Diagnostics of the true (ψ_3) and predicted ($\tilde{\psi}_3$) bottom-layer streamfunction are
 587 shown in Figure 8f-j. Despite a moderate correlation of $r \approx 0.5$ across the domain, the
 588 predictions fail to reproduce the correct time-mean, which has a circulation in the op-
 589 posite direction to the truth. This is due to the neural network being trained to predict
 590 the middle-layer flow, which on average is more aligned with the upper-layer. Therefore
 591 when the neural network is given the middle-layer streamfunction as an input, it pre-
 592 dicts the bottom-layer flow as on-average being in the same direction, which is not the
 593 case. The neural network also hasn't been trained to predict the effects of the additional
 594 bottom drag, decreasing the accuracy further - more data could improve this issue, as
 595 the longer time scales associated with bottom drag may be absent from the training dataset.

596 An alternative approach would be to train a new neural network to map directly
 597 from the surface flow to the bottom-layer flow, i.e., $\tilde{\psi}_3 = f(\bar{\psi}_1, \mathbf{W})$. Having separate neu-
 598 ral networks for the middle- and bottom-layers, you could then reconstruct the flow at
 599 all depths using just information at the surface (although an additional neural network
 600 does increase computational costs). Independent of the abyssal flow however, we have
 601 shown that neural networks can provide information on the flow at intermediate depths.

602 7 Conclusions & Discussion

603 7.1 Summary

604 In this study, we have demonstrated as a proof-of-concept that machine learning
 605 algorithms can provide information on unresolved turbulent processes, when given a smoothed-
 606 view of the dynamics (i.e. the filtered-streamfunction). We degrade data from a high-
 607 resolution eddy-resolving QG model using a spatial low-pass filter, and train convolu-
 608 tional neural networks to predict the relationship between turbulent processes and their
 609 effect on the large-scale flow, i.e. the eddy momentum forcing. Our results show that con-
 610 volutional neural networks can successfully represent both the spatial and temporal vari-
 611 ability of the eddy momentum forcing.

612 We determine how neural networks trained on one area of the domain, perform in
 613 other previously-unseen areas (Figures 2 and 3), representing when observational data
 614 is limited to only particular regions, for example mooring data [Hogg, 1992] or gliders
 615 [Rudnick et al., 2004; Davis et al., 2008]. Training on a sub-region tests the sensitivity
 616 of the neural network performance to the underlying physical processes. We find that
 617 the region on which the neural network is trained significantly impacts the accuracy, as
 618 well as the mean-bias which impacts momentum conservation. In particular, training on

619 the least energetically active region, the southern gyre, leads to the lowest accuracy; these
 620 neural networks could not reproduce the variability in more energetic regions, such as
 621 within the meandering jet. However, training on the western boundary leads to the best
 622 generalisation, in terms of reproducing the correct amplitude of the eddy momentum forc-
 623 ing in the rest of the domain.

624 The variation in performance between regions implies that training on the most
 625 turbulent region leads to the best performing neural networks for eddy momentum forc-
 626 ing prediction. It is possible that data from the most turbulent regions exhibits the high-
 627 est variance, or contains a more diverse range of scale-interactions. However, two regions
 628 may be as turbulent or energetically active as each other, but the nature of the eddy-
 629 mean flow interactions within them may differ. For example, *Waterman and Jayne* [2010]
 630 showed that in an idealised model the effect of eddies on the mean-flow depended crit-
 631 ically on along-stream position: up-stream eddies are generated by an unstable jet, while
 632 down-stream the eddies drive the time-mean circulation. Therefore training neural net-
 633 works on different along-stream positions may lead to different dynamical-processes be-
 634 ing learnt, despite both regions being energetically active. Here we have shown how the
 635 performance varies between regions of differing energetic activity, but how the specific
 636 effects of eddies- e.g. driving the mean-flow, versus eddies extracting momentum and en-
 637 ergy from the jet -impacts the neural network performance remains to be determined.

638 Without further training, we show that a neural network trained on one QG model
 639 configuration generalises exceedingly well to QG models with different viscosity coeffi-
 640 cients and wind forcings (Figure 4). The neural network within the jet reproduces the
 641 correct spatio-temporal variability (<10% error) in all configurations, and the more tur-
 642 bulent the configuration, the better the correlation between the predicted \tilde{S}_x and the true
 643 S_x within the gyres. While the neural networks do not conserve momentum globally (Fig-
 644 ure 5c and 5d), we show that momentum conservation can be enforced without a sig-
 645 nificant reduction in accuracy (Figure 6), through either a physically-constrained archi-
 646 tecture or post-processing of the predictions.

647 We also show that a new neural network can be trained to predict the middle-layer
 648 streamfunction, using only the upper-layer streamfunction as the input, i.e., predicting
 649 the flow at depth using information at the surface (Figure 8). The highest accuracy oc-
 650 curs where the barotropic component of the flow is most dominant, which coincides with
 651 a strong zonal mean-flow. However, when using the streamfunction to predict the bottom-
 652 layer streamfunction, the neural network captures some of the variability, but fails to repli-
 653 cate the time-mean of the true bottom-layer streamfunction ψ_3 (Figure 8), primarily due
 654 to the presence of bottom-drag.

655 7.2 Implications for leveraging observations

656 Our work has implications for inference from sparse observations. While previous
 657 studies have used machine learning to leverage observational datasets [*Chapman and Cha-*
 658 *rantonis*, 2017; *Su et al.*, 2018; *Giglio et al.*, 2018], the present work demonstrates that
 659 convolutional neural networks in particular are an excellent tool for such tasks. Neural
 660 networks should be further tested and exploited in the future for data inference due to

- 661 • their resilience, such that accurate predictions for the full domain can be gener-
 662 ated by training on a sub-region.
- 663 • their generalisation to different external forcings, without any further training such
 664 that predictions outside the regime trained on can be successful.
- 665 • their ability to be successfully trained with under-sampled data. (Figure 7).

666 Collectively, these results suggest that sparse interpolated observational datasets
 667 can be leveraged by such data-driven techniques. For example, satellite altimetry data

668 can be used to predict the sub-surface flow; or data from moorings deployed in Drake
 669 Passage as part of the Diapycnal and Isopycnal Mixing Experiment in the Southern Ocean
 670 (DIMES) can be used to infer eddy momentum or heat flux divergences in other parts
 671 of the Southern Ocean. In addition, datasets from Argo floats [Chapman and Sallée, 2017],
 672 mooring data, ADCPs, and SSH from altimetry, could be combined to reconstruct physically-
 673 and biogeochemically important quantities such energy reservoirs, or air-sea fluxes, in-
 674 terior transport and/or storage of heat, carbon and oxygen in the ocean [Su et al., 2018;
 675 Giglio et al., 2018].

676 7.3 Implications for parametrizations

677 Although we have motivated our study through the leverage of observations and
 678 coarse-resolution model data, our results have implications for eddy parameterisations
 679 of momentum, and more generally for sub-grid parametrizations. As discussed previously,
 680 machine learning has been used to parameterise unresolved processes in the atmosphere
 681 [Brenowitz and Bretherton, 2018; Jiang et al., 2018; Gentine et al., 2018; O’Gorman and
 682 Dwyer, 2018]. We have shown that neural networks can successfully represent the spatio-
 683 temporal variability of the eddy momentum forcing, implying potential for data-driven
 684 oceanic turbulence closures in the future. The generalisation ability of the neural net-
 685 works shows that only a limited amount of observations or high-resolution model data
 686 may be needed to successfully represent sub-grid scale processes. While the CNNs are
 687 successful at representing relationship between the eddy momentum forcing and their
 688 effect on the resolved flow, the low-resolution climate models might have biases that are
 689 too severe (e.g., weak transport and velocity shears) to lead to a successful representa-
 690 tion of the eddy momentum forcing from CNNs as trained here. Yet, our results also show
 691 that they perform very well for different forcing and dissipation terms, therefore until
 692 the CNNs are implemented into a coarse-resolution ocean model, their success in improv-
 693 ing numerical simulations is purely speculative but deserves to be investigated.

694 Whether neural networks are being used to leverage observations, or more impor-
 695 tantly to construct a data-driven eddy parameterisation, caution must be taken to en-
 696 sure that the laws of physics are respected. More work into physically-constrained ma-
 697 chine learning algorithms is crucial, and successful applications of data-driven techniques
 698 should incorporate physical knowledge. Indeed, the neural network turbulence model of
 699 Ling et al. [2016b] out-performed more simple linear models only when Galilean invari-
 700 ant stress tensors from Pope [1975] were used, which are also a key ingredient of the eddy
 701 parameterisation proposed by Anstey and Zanna [2017]. As previously discussed, we suc-
 702 cessfully enforce global momentum conservation in the present work, such that future
 703 implementations of data-driven parameterisations, despite being semi-empirical, can be
 704 altered to respect physical principles. Specifically, physical constraints can be incorpo-
 705 rated into the architecture of the predictive algorithms.

706 One disadvantage of convolutional neural networks is the computational cost of the
 707 matrix operations of each convolution layer to make a prediction given an input. The
 708 total time complexity (ignoring any fully-connected layers) of a CNN [He and Sun, 2015]
 709 is given by $\mathcal{O}(\sum_l^d n_{l-1} \cdot s_l^2 \cdot n_l \cdot m_l^2)$, where d is the total number of convolution layers, l
 710 is the index of a convolution layer, n_l is the number of filters, s_l is the filter size, and m_l
 711 is the size of the output feature map. The time complexity is larger than that of a tra-
 712 ditional eddy closure (e.g., a simple laplacian dissipation of momentum which only in-
 713 volves a few matrix additions and subtractions). One way to reduce the time complex-
 714 ity is to instead use depth-wise separable convolution layers [Howard et al., 2017, e.g],
 715 which treat the input channels of a convolution layer more independently. This reduces
 716 the number of parameters and hence computational cost. An alternative way of reduc-
 717 ing time complexity is to simply reduce the sizes of the input and outputs, i.e. make pre-
 718 dictions for a region smaller than 40×40 grid points. The amount of information avail-
 719 able to make predictions is therefore reduced. The computational cost is an area which

needs addressing if CNNs are to be routinely implemented in models in the future. However, unlike other parametrizations, the training of the neural networks is only done once.

7.4 Future Work

Our study is a step towards using convolutional neural networks to extend the reach of currently available observational or model data. Our proof-of-concept study was conducted in an idealised QG model. The next stage involves training neural networks on actual observational datasets (as described in Section 7.2) or on more realistic model data (e.g. a 1/40th degree global model which resolves the mesoscale and submesoscale eddy fields, such as in *Rocha et al.* [2016]).

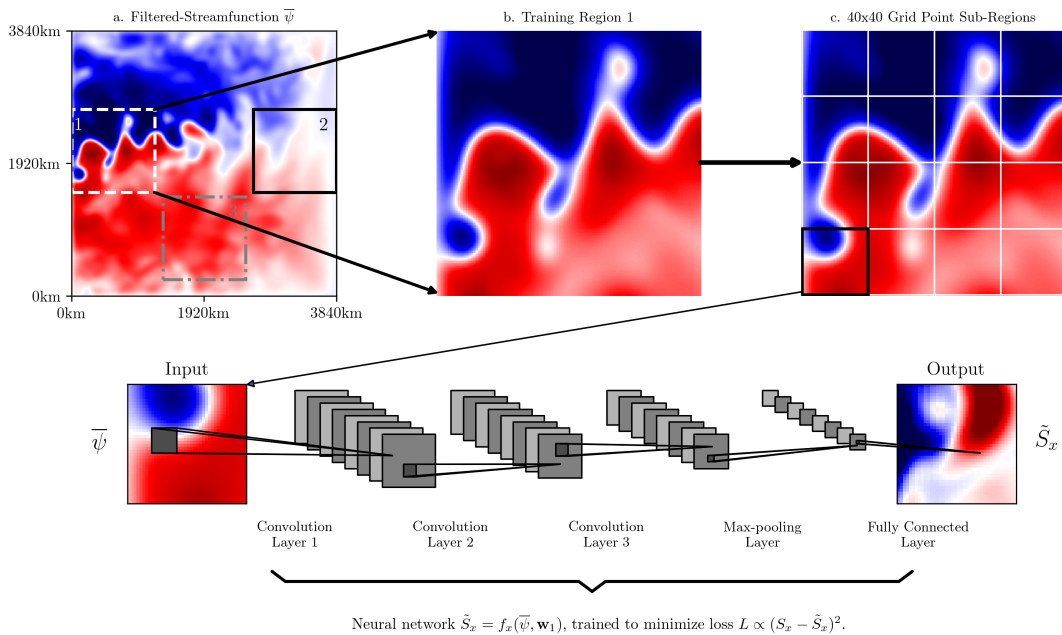
We used nine years of data to train the neural networks, and one year for validation. *Gentine et al.* [2018] showed, with regards to parameterising convection with neural networks, that the training dataset could be reduced in size from 12 months to 3 months, with little change in the overall mean-squared error. The sensitivity our neural networks to reductions in the amount of training data needs to be systematically explored. We have only determined the impact of spatial under-sampling on the neural networks. However, further work is needed to determine the impact of using a few number of time-slices (e.g. using 3 years of training data as opposed to 9 years used here).

Training on the western boundary produces the best performance. However, the high skill within the jet does not fully translate to high skill in all parts of the gyres. The best correlations in the gyres occurs instead when training on the southern gyre, and not the western or eastern boundaries (Figure 2 and 3). This implies there may be an optimal combination of the predictions of the neural networks trained on different regions, in order to produce the best overall generalisation and potentially include non-local effects. E.g., each neural network has a weight a_i , and the optimal predictions for the full domain is a combination of all neural networks

$$\tilde{S}_x^{OPT} = \sum_i^N a_i f_x(\bar{\psi}, \mathbf{w}_i), \quad (10)$$

where the summation is over all regions, and \tilde{S}_x^{OPT} is the corresponding optimal prediction (with an analogous \tilde{S}_y^{OPT} for the meridional component). Combining predictions from multiple neural networks in this manner could be a useful way of capturing the distinct eddy-mean flow interactions observed by *Waterman and Jayne* [2010]. Alternatively, if the computational resources are available, you could train a single neural network on data from all three regions, in the hope that it ‘remembers’ the physical processes occurring in each region. The risk with this approach is that one loses specialisation, and the skill reduces as the single neural network simply ‘averages’ the effects of the three regions together. We will attempt to implement the neural networks (as trained here, or as a combination of neural networks) into a coarse resolution version of the QG model to test their performance as a sub-grid scale parametrization.

Although this study is a proof-of-concept, the merging of data-driven methods with physical knowledge has the potential to change the way the physics of the ocean are studied in the future. The combination of physical theory and machine learning could prove more effective than either component in isolation.



760 **Figure 1.** Panel (a) illustrates the upper-layer filtered-streamfunction $\bar{\psi}$ of the QG model,
 761 including the three regions in which we train the neural networks: region 1 (white-dashed)
 762 is on the western boundary, region 2 (black-solid) is on the eastern boundary, and region 3
 763 (grey-dash-dotted) is centered on the southern gyre. Panel (b) shows a close-up of the filtered-
 764 streamfunction $\bar{\psi}$ within training region 1 while Panel (c) illustrates how training region 1 is
 765 split into 16 40×40 grid point sub-regions - the size of the input and output arrays of the neural
 766 network is 40×40 grid points. The input variable of each neural network is the filtered stream-
 767 function $\bar{\psi}$, and the output variable is either the zonal component \tilde{S}_x or meridional component
 768 \tilde{S}_y of the sub-filter eddy momentum forcing. The architecture of the convolutional neural net-
 769 work, with an example input $\bar{\psi}$ and output \tilde{S}_x , is illustrated underneath Panels (a), (b), and (c).

812 Acknowledgments

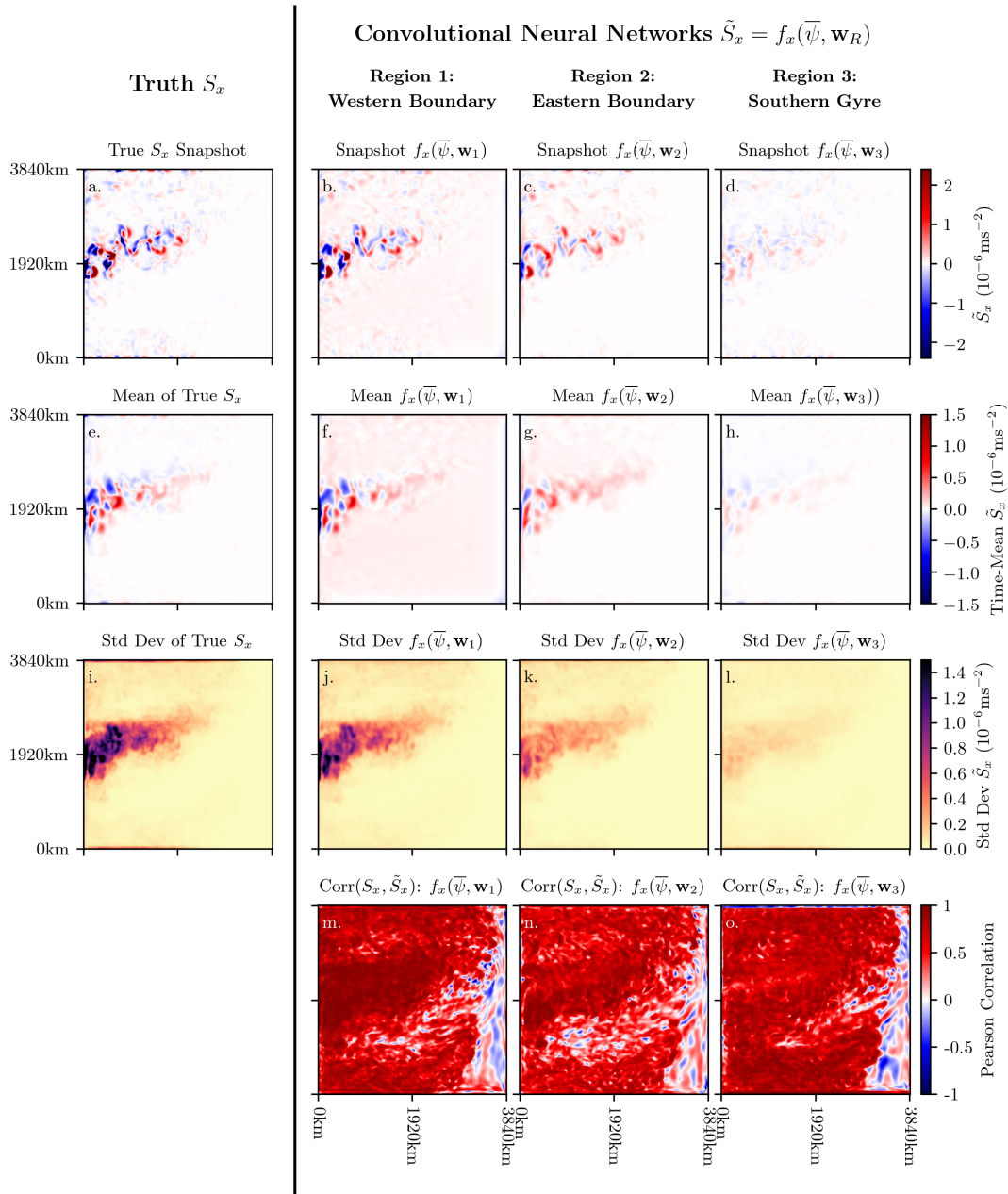
813 This study was funded by the Natural Environment Research Council (NERC). We thank
 814 PierGianLuca Porta Mana, who conducted the high-resolution PEQUOD model simu-
 815 lations. Thank you to Robert Fraser, Tomos David, and Ryan Abernathey for their help-
 816 ful discussions during the development of this work, and to two anonymous reviewers
 817 for their comments which helped improve this manuscript. The trained Keras neural net-
 818 works, their training histories, and the Python code used to produce this paper, can all
 819 be found in the following GitHub repository: <https://github.com/TomBolton/DeepEddy>.

820 References

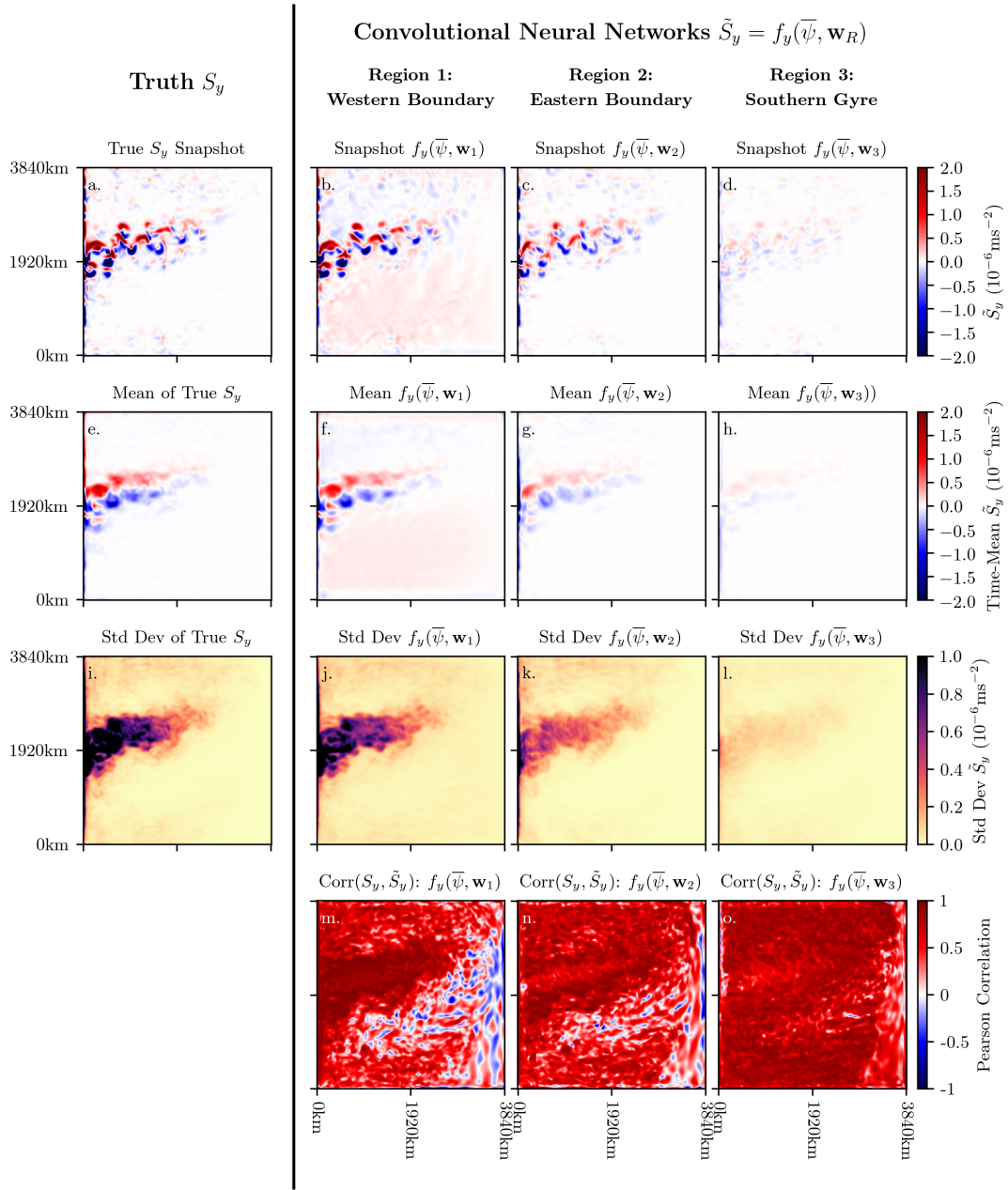
- 821 Abadi, M., P. Barham, J. Chen, Z. Chen, A. Davis, J. Dean, M. Devin, S. Ghe-
 822 mawat, G. Irving, M. Isard, et al. (2016), Tensorflow: A system for large-scale
 823 machine learning., in *OSDI*, vol. 16, pp. 265–283.
- 824 Abernathey, R. P., and J. Marshall (2013), Global surface eddy diffusivities derived
 825 from satellite altimetry, *Journal of Geophysical Research: Oceans*, *118*(2), 901–
 826 916.
- 827 Anderson, G. J., and D. D. Lucas (2018), Machine learning predictions of a multires-
 828 olution climate model ensemble, *Geophysical Research Letters*, *45*(9), 4273–4280.

Quasi-Geostrophic Model Parameters	
Domain size (grid points)	512×512
Domain length (L)	3840 km
Resolution (Δx)	7.5 km
Viscosity (ν)	75 m ² s ⁻¹
Rosby deformation radii (L_{Ro})	40,23 km
Velocity scale ($\sqrt{EK\bar{E}}$)	0.21 ms ⁻¹
Planetary vorticity (f_0)	10 ⁻⁴ s ⁻¹
Rosby parameter (β)	2 * 10 ⁻¹¹ m ⁻¹ s ⁻¹
Gravity (g)	9.8 ms ⁻²
Reduced gravity (g')	0.034, 0.018 ms ⁻²
Bottom drag coefficient (r)	4 * 10 ⁻⁸ s ⁻¹
Wind stress amplitude (τ_0)	0.8 Nm ⁻²
Reference density (ρ_0)	10 ³ kgm ⁻³
Neural Network Data Details	
Data source	Quasi-geostrophic ocean model
Input variable (feature)	Filtered streamfunction $\bar{\psi}$
Output variables (targets)	Sub-filter momentum forcing S_x, S_y
Training Region 1	Western boundary
Training Region 2	Eastern boundary
Training Region 3	Southern gyre
Number of training samples	52800 (years 1-9)
Number of validation samples	5600 (year 10)
Standardisation method	Zero mean, unit variance
Neural Network Architecture	
Input size	40×40
Number of convolution layers	3
Number of filters for each convolution layer	16, 16*8, 8*8
Size of filter for each convolution layer	8×8, 4×4, 4×4
Filter stride for each convolution layer	2, 1, 1
Activation function for each convolution layer	SELU, SELU, SELU
Max pooling kernel size	2
Output layer activation function	None/Linear
Output size	40×40
Neural Network Training Parameters	
Loss function	Mean-square error
Optimiser	Adam
Learning rate	0.001
Momentum	0.9
Batch size	16
Training epochs	200

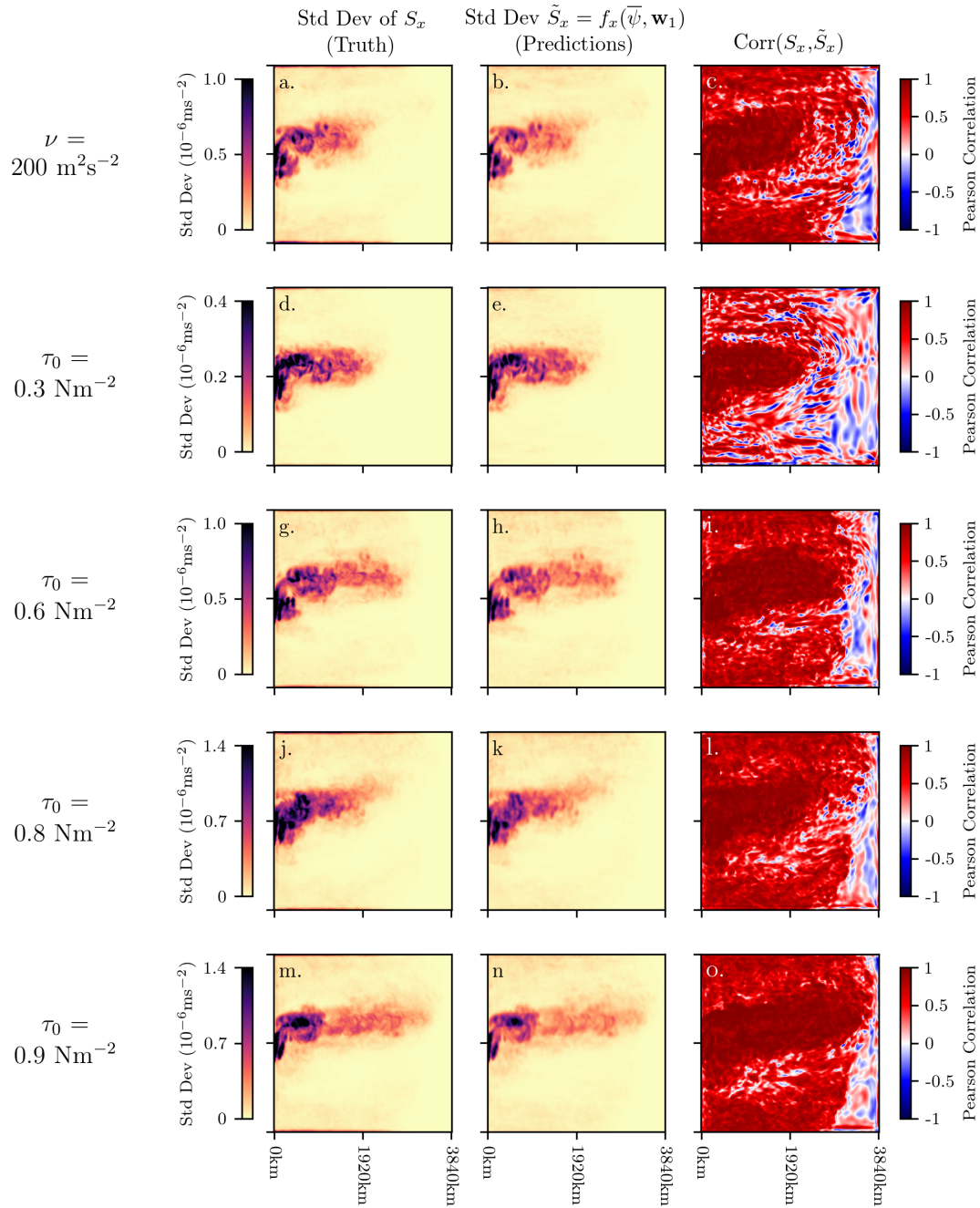
770 **Table 1.** Details on the following: the quasi-geostrophic ocean model parameters, the datasets
771 used to train the neural networks, the architecture parameters, and the optimisation parameters.



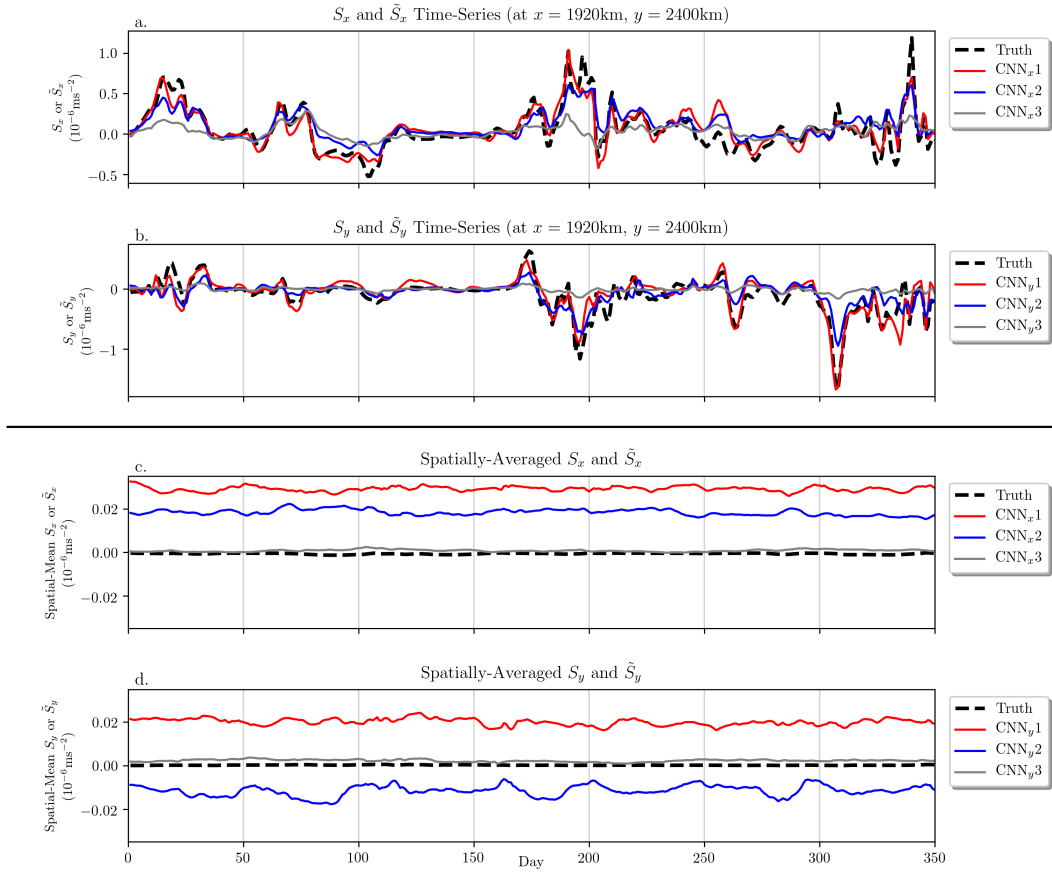
772 **Figure 2.** Examining the non-local prediction ability. Comparisons of the true zonal component of the sub-filter momentum forcing S_x , with the neural networks trained using data from
 773 three different regions. The first three rows compare snapshots, time-means, and the standard
 774 deviation respectively, while the bottom row shows the correlation between the true S_x and the
 775 predictions \tilde{S}_x . The first column contains the diagnostics using the true zonal sub-filter momentum
 776 forcing S_x , while columns two, three, and four use predictions \tilde{S}_x from the neural networks
 777 $f_x(\bar{\psi}, \mathbf{w}_1)$, $f_x(\bar{\psi}, \mathbf{w}_2)$, and $f_x(\bar{\psi}, \mathbf{w}_3)$ respectively. All diagnostics were produced using the validation
 778 data.
 779



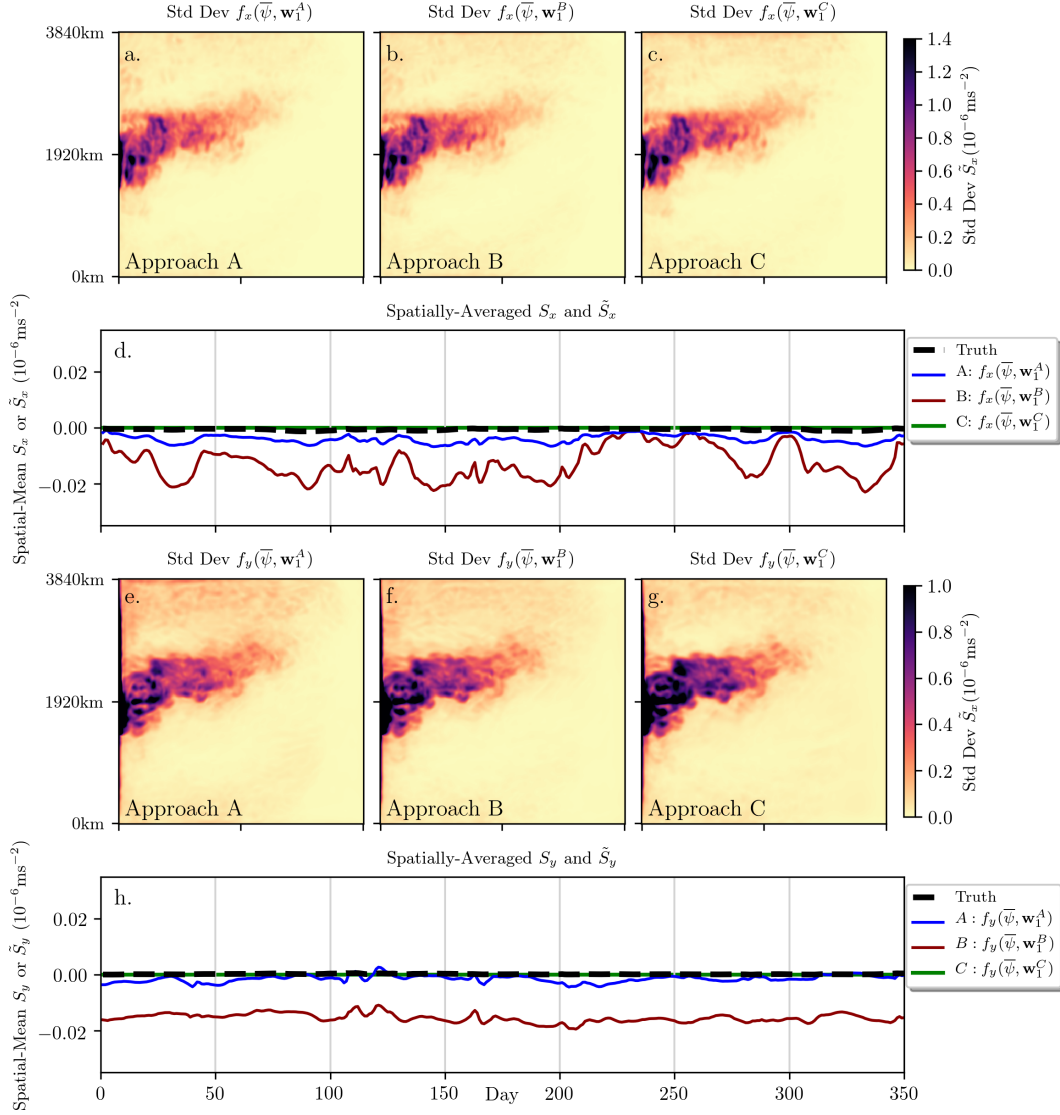
780 **Figure 3.** The same diagnostics as Figure 2, but for the meridional component of the sub-
 781 filter momentum forcing: the true S_y and the predictions \tilde{S}_y from the neural networks $f_y(\bar{\psi}, \mathbf{w}_1)$,
 782 $f_y(\bar{\psi}, \mathbf{w}_2)$, and $f_y(\bar{\psi}, \mathbf{w}_3)$.



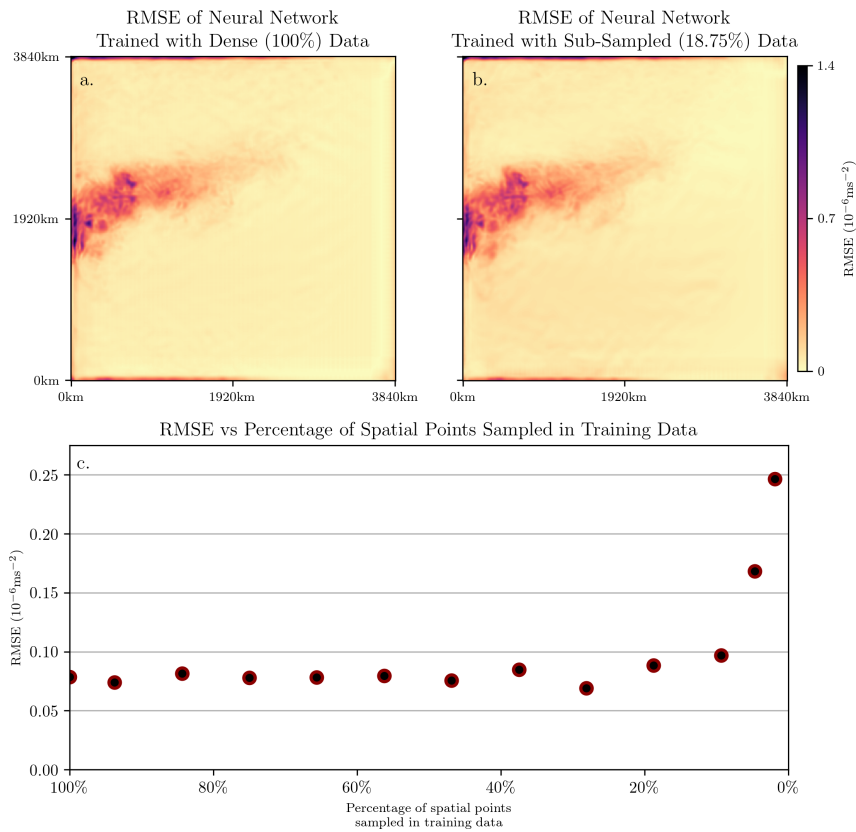
783 **Figure 4.** Examining the ability to generalise to new regimes: using the trained neural net-
 784 work $f_x(\bar{\psi}, \mathbf{w}_1)$, we make predictions for model runs of different viscosities and wind forcings.
 785 From each model run, we use one year of the upper-layer filtered streamfunction to generate
 786 predictions \tilde{S}_x from $f_x(\bar{\psi}, \mathbf{w}_1)$ to see how they compare to the true S_x . We study a run of higher
 787 viscosity $\nu = 200 \text{ m}^2\text{s}^{-2}$, and runs with wind stress amplitude $\tau_0 = 0.3, 0.6, 0.8,$ and 0.9 Nm^{-2} .
 788 Note that $f_x(\bar{\psi}, \mathbf{w}_1)$ was trained on a run with $\nu = 75 \text{ m}^2\text{s}^{-2}$ and $\tau_0 = 0.8 \text{ Nm}^{-2}$, the standard
 789 deviation and correlation maps of which are included again here in Panels (j), (k), and (l).



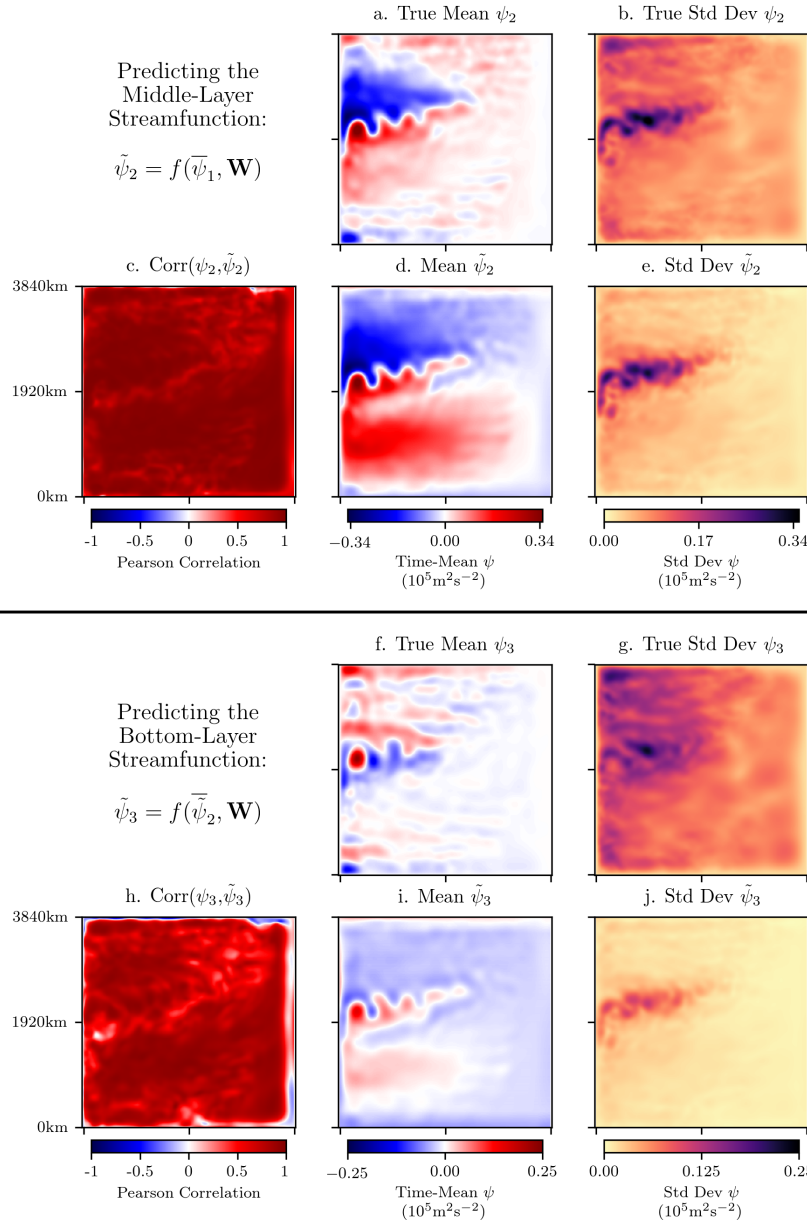
790 **Figure 5.** Panels (a) and (b) show time series of the zonal and meridional components of
 791 the sub-filter momentum forcing respectively, at a single point near the middle of the domain.
 792 Panels (c) and (d) also show time series of the zonal and meridional components of the sub-filter
 793 momentum forcing, but this time spatially-averaged over the entire domain.



794 **Figure 6.** The standard deviation and spatial-average time series of the predictions \tilde{S}_x and
 795 \tilde{S}_y of the momentum conserving approaches A, B, and C. Panels (a), (b), and (c) show the
 796 standard deviation of \tilde{S}_x from $f_x(\bar{\psi}, \mathbf{w}_1^A)$, $f_x(\bar{\psi}, \mathbf{w}_1^B)$, and $f_x(\bar{\psi}, \mathbf{w}_1^C)$ respectively, while Pan-
 797 els (e), (f), and (g) show the standard deviation of \tilde{S}_y from $f_y(\bar{\psi}, \mathbf{w}_1^A)$, $f_y(\bar{\psi}, \mathbf{w}_1^B)$, and $f_y(\bar{\psi}, \mathbf{w}_1^C)$
 798 respectively. The spatial-averages of these predictions \tilde{S}_x and \tilde{S}_y are shown in Panels (d) and (h).



799 **Figure 7.** Determining how under-sampling of the training data impacts neural network error.
 800 Panel (a) shows the RMSE of the neural network $f_x(\bar{\psi}, \mathbf{w}_1)$ trained with dense (un-altered)
 801 training data, while Panel (b) shows the RMSE of the neural network trained with sub-sampled
 802 (18.75%) data. Panel (c) shows the RMSE as a function of the percentage of spatial points
 803 sampled at each time-slice of the training data. Note that the RMSE is calculated over the full-
 804 domain during the validation period (the final year of data).



805 **Figure 8.** Predicting the middle- and bottom-layer streamfunctions ψ_2 and ψ_3 using the
 806 upper-layer filtered streamfunction $\bar{\psi}_1$. We first train a new neural network to predict ψ_2 from
 807 $\bar{\psi}_1$, i.e., $\psi_2 = f(\bar{\psi}_1, \mathbf{W})$; diagnostics of the true ψ_2 and the predictions $\tilde{\psi}_2$ are shown in the top-
 808 half of the Figure. We then take the same neural network that was trained to predict ψ_2 from
 809 $\bar{\psi}_1$, and now predict the bottom layer streamfunction ψ_3 using the predicted middle-layer stream-
 810 function as the input, i.e., $\psi_3 = f(\tilde{\psi}_2, \mathbf{W})$; the diagnostics of the true ψ_3 and the predictions $\tilde{\psi}_3$
 811 are shown in the bottom-half of the Figure.

- 829 Anstey, J. A., and L. Zanna (2017), A deformation-based parametrization of ocean
830 mesoscale eddy reynolds stresses, *Ocean Modelling*, *112*, 99–111.
- 831 Arbic, B. K., K. L. Polzin, R. B. Scott, J. G. Richman, and J. F. Shriver (2013), On
832 eddy viscosity, energy cascades, and the horizontal resolution of gridded satellite
833 altimeter products, *Journal of Physical Oceanography*, *43*(2), 283–300.
- 834 Berloff, P. S. (2005), On dynamically consistent eddy fluxes, *Dynamics of atmo-*
835 *spheres and oceans*, *38*(3-4), 123–146.
- 836 Brenowitz, N. D., and C. S. Bretherton (2018), Prognostic validation of a neural
837 network unified physics parameterization, *Geophysical Research Letters*.
- 838 Chapman, C., and A. A. Charantonis (2017), Reconstruction of subsurface velocities
839 from satellite observations using iterative self-organizing maps, *IEEE Geoscience*
840 *and Remote Sensing Letters*, *14*(5), 617–620.
- 841 Chapman, C., and J.-B. Sallée (2017), Can we reconstruct mean and eddy fluxes
842 from argo floats?, *Ocean Modelling*, *120*, 83–100.
- 843 Chelton, D. B., M. G. Schlax, R. M. Samelson, and R. A. de Szoeke (2007), Global
844 observations of large oceanic eddies, *Geophysical Research Letters*, *34*(15).
- 845 Chollet, F., et al. (2015), Keras, <https://keras.io>.
- 846 Davis, R. E., M. D. Ohman, D. L. Rudnick, and J. T. Sherman (2008), Glider
847 surveillance of physics and biology in the southern california current system,
848 *Limnology and Oceanography*, *53*(5part2), 2151–2168.
- 849 Dong, C., C. C. Loy, K. He, and X. Tang (2016), Image super-resolution using deep
850 convolutional networks, *IEEE transactions on pattern analysis and machine intel-*
851 *ligence*, *38*(2), 295–307.
- 852 Durand, M., L.-L. Fu, D. P. Lettenmaier, D. E. Alsdorf, E. Rodriguez, and
853 D. Esteban-Fernandez (2010), The surface water and ocean topography mission:
854 Observing terrestrial surface water and oceanic submesoscale eddies, *Proceedings*
855 *of the IEEE*, *98*(5), 766–779.
- 856 Esteves, J. T., G. de Souza Rolim, and A. S. Ferraudo (2018), Rainfall prediction
857 methodology with binary multilayer perceptron neural networks, *Climate Dynam-*
858 *ics*, pp. 1–13.
- 859 Gentine, P., M. Pritchard, S. Rasp, G. Reinaudi, and G. Yacalis (2018), Could
860 machine learning break the convection parameterization deadlock?, *Geophysical*
861 *Research Letters*.
- 862 Giglio, D., V. Lyubchich, and M. Mazloff (2018), Estimating oxygen in the south-
863 ern ocean using argo temperature and salinity, *Journal of Geophysical Research:*
864 *Oceans*.
- 865 Goodfellow, I., Y. Bengio, A. Courville, and Y. Bengio (2016), *Deep learning*, vol. 1,
866 MIT press Cambridge.
- 867 Greatbatch, R., X. Zhai, M. Claus, L. Czeschel, and W. Rath (2010a), Transport
868 driven by eddy momentum fluxes in the gulf stream extension region, *Geophysical*
869 *Research Letters*, *37*(24).
- 870 Greatbatch, R. J., X. Zhai, J.-D. Kohlmann, and L. Czeschel (2010b), Ocean eddy
871 momentum fluxes at the latitudes of the gulf stream and the kuroshio extensions
872 as revealed by satellite data, *Ocean Dynamics*, *60*(3), 617–628.
- 873 Hallberg, R. (2013), Using a resolution function to regulate parameterizations of
874 oceanic mesoscale eddy effects, *Ocean Modelling*, *72*, 92–103.
- 875 He, K., and J. Sun (2015), Convolutional neural networks at constrained time cost,
876 in *Proceedings of the IEEE conference on computer vision and pattern recognition*,
877 pp. 5353–5360.
- 878 Hewitt, H. T., M. J. Roberts, P. Hyder, T. Graham, J. Rae, S. E. Belcher,
879 R. Bourdallé-Badie, D. Copey, A. Coward, C. Guiavarch, et al. (2016), The
880 impact of resolving the rossby radius at mid-latitudes in the ocean: Results from
881 a high-resolution version of the met office gc2 coupled model, *Geoscientific Model*
882 *Development*, *9*(10), 3655–3670.

- 883 Hogg, N. G. (1992), On the transport of the gulf stream between cape hatteras and
 884 the grand banks, *Deep Sea Research Part A. Oceanographic Research Papers*,
 885 *39*(7-8), 1231–1246.
- 886 Howard, A. G., M. Zhu, B. Chen, D. Kalenichenko, W. Wang, T. Weyand, M. An-
 887 dreetto, and H. Adam (2017), Mobilenets: Efficient convolutional neural networks
 888 for mobile vision applications, *arXiv preprint arXiv:1704.04861*.
- 889 Jiang, G.-Q., J. Xu, and J. Wei (2018), A deep-learning algorithm of neural network
 890 for the parameterization of typhoon–ocean feedback in typhoon forecast models,
 891 *Geophysical Research Letters*.
- 892 Jochum, M., G. Danabasoglu, M. Holland, Y.-O. Kwon, and W. Large (2008), Ocean
 893 viscosity and climate, *Journal of Geophysical Research: Oceans*, *113*(C6).
- 894 Kang, D., and E. N. Curchitser (2015), Energetics of eddy–mean flow interactions in
 895 the gulf stream region, *Journal of Physical Oceanography*, *45*(4), 1103–1120.
- 896 Keating, S. R., and K. S. Smith (2015), Upper ocean flow statistics estimated from
 897 superresolved sea-surface temperature images, *Journal of Geophysical Research:*
 898 *Oceans*, *120*(2), 1197–1214.
- 899 Keating, S. R., A. J. Majda, and K. S. Smith (2012), New methods for estimating
 900 ocean eddy heat transport using satellite altimetry, *Monthly Weather Review*,
 901 *140*(5), 1703–1722.
- 902 Kingma, D. P., and J. Ba (2014), Adam: A method for stochastic optimization,
 903 *arXiv preprint arXiv:1412.6980*.
- 904 Kjellsson, J., and L. Zanna (2017), The impact of horizontal resolution on energy
 905 transfers in global ocean models, *Fluids*, *2*(3), 45.
- 906 Klambauer, G., T. Unterthiner, A. Mayr, and S. Hochreiter (2017), Self-normalizing
 907 neural networks, in *Advances in Neural Information Processing Systems*, pp. 972–
 908 981.
- 909 Krizhevsky, A., I. Sutskever, and G. E. Hinton (2012), Imagenet classification with
 910 deep convolutional neural networks, in *Advances in neural information processing*
 911 *systems*, pp. 1097–1105.
- 912 Kutz, J. N. (2017), Deep learning in fluid dynamics, *Journal of Fluid Mechanics*,
 913 *814*, 1–4.
- 914 Le Traon, P., and R. Morrow (2001), Ocean currents and eddies, in *International*
 915 *Geophysics*, vol. 69, pp. 171–xi, Elsevier.
- 916 Le Traon, P., F. Nadal, and N. Ducet (1998), An improved mapping method of mul-
 917 tisatellite altimeter data, *Journal of atmospheric and oceanic technology*, *15*(2),
 918 522–534.
- 919 LeCun, Y., Y. Bengio, and G. Hinton (2015), Deep learning, *nature*, *521*(7553), 436.
- 920 Ling, J., R. Jones, and J. Templeton (2016a), Machine learning strategies for sys-
 921 tems with invariance properties, *Journal of Computational Physics*, *318*, 22–35.
- 922 Ling, J., A. Kurzawski, and J. Templeton (2016b), Reynolds averaged turbulence
 923 modelling using deep neural networks with embedded invariance, *Journal of Fluid*
 924 *Mechanics*, *807*, 155–166.
- 925 Mana, P. P., and L. Zanna (2014), Toward a stochastic parameterization of ocean
 926 mesoscale eddies, *Ocean Modelling*, *79*, 1–20.
- 927 McGovern, A., K. L. Elmore, D. J. Gagne, S. E. Haupt, C. D. Karstens,
 928 R. Lagerquist, T. Smith, and J. K. Williams (2017), Using artificial intelligence
 929 to improve real-time decision-making for high-impact weather, *Bulletin of the*
 930 *American Meteorological Society*, *98*(10), 2073–2090.
- 931 Moeng, C.-H. (1984), A large-eddy-simulation model for the study of planetary
 932 boundary-layer turbulence, *Journal of the Atmospheric Sciences*, *41*(13), 2052–
 933 2062.
- 934 Morrow, R., R. Coleman, J. Church, and D. Chelton (1994), Surface eddy momen-
 935 tum flux and velocity variances in the southern ocean from geosat altimetry,
 936 *Journal of Physical Oceanography*, *24*(10), 2050–2071.

- 937 O’Gorman, P. A., and J. G. Dwyer (2018), Using machine learning to parameterize
938 moist convection: potential for modeling of climate, climate change and extreme
939 events, *Journal of Advances in Modelling Earth Systems*.
- 940 Pathak, J., B. Hunt, M. Girvan, Z. Lu, and E. Ott (2018a), Model-free prediction
941 of large spatiotemporally chaotic systems from data: a reservoir computing ap-
942 proach, *Physical review letters*, *120*(2), 024,102.
- 943 Pathak, J., A. Wikner, R. Fussell, S. Chandra, B. R. Hunt, M. Girvan, and E. Ott
944 (2018b), Hybrid forecasting of chaotic processes: using machine learning in con-
945 junction with a knowledge-based model, *Chaos: An Interdisciplinary Journal of*
946 *Nonlinear Science*, *28*(4), 041,101.
- 947 Pope, S. (1975), A more general effective-viscosity hypothesis, *Journal of Fluid*
948 *Mechanics*, *72*(2), 331–340.
- 949 Rocha, C. B., S. T. Gille, T. K. Chereskin, and D. Menemenlis (2016), Seasonality
950 of submesoscale dynamics in the kuroshio extension, *Geophysical Research Letters*,
951 *43*(21), 11–304.
- 952 Roemmich, D., G. C. Johnson, S. Riser, R. Davis, J. Gilson, W. B. Owens, S. L.
953 Garzoli, C. Schmid, and M. Ignaszewski (2009), The argo program: Observing the
954 global ocean with profiling floats, *Oceanography*, *22*(2), 34–43.
- 955 Rudnick, D. L., R. E. Davis, C. C. Eriksen, D. M. Fratantoni, and M. J. Perry
956 (2004), Underwater gliders for ocean research, *Marine Technology Society Journal*,
957 *38*(2), 73–84.
- 958 Sagaut, P. (2006), *Large eddy simulation for incompressible flows: an introduction*,
959 Springer Science & Business Media.
- 960 Scott, R. B., and F. Wang (2005), Direct evidence of an oceanic inverse kinetic en-
961 ergy cascade from satellite altimetry, *Journal of Physical Oceanography*, *35*(9),
962 1650–1666.
- 963 Simonyan, K., and A. Zisserman (2014), Very deep convolutional networks for large-
964 scale image recognition, *arXiv preprint arXiv:1409.1556*.
- 965 Su, H., W. Li, and X.-H. Yan (2018), Retrieving temperature anomaly in the global
966 subsurface and deeper ocean from satellite observations, *Journal of Geophysical*
967 *Research: Oceans*, *123*(1), 399–410.
- 968 Tracey, B. D., K. Duraisamy, and J. J. Alonso (2015), A machine learning strat-
969 egy to assist turbulence model development, in *53rd AIAA Aerospace Sciences*
970 *Meeting*, p. 1287.
- 971 Vlachas, P. R., W. Byeon, Z. Y. Wan, T. P. Sapsis, and P. Koumoutsakos (2018),
972 Data-driven forecasting of high-dimensional chaotic systems with long short-term
973 memory networks, *Proc. R. Soc. A*, *474*(2213), 20170,844.
- 974 Waterman, S., and S. R. Jayne (2010), Eddy-mean flow interactions in the along-
975 stream development of a western boundary current jet: An idealized model study,
976 *Journal of Physical Oceanography*.
- 977 Waterman, S., N. G. Hogg, and S. R. Jayne (2011), Eddy-mean flow interaction in
978 the kuroshio extension region, *Journal of Physical Oceanography*, *41*(6), 1182–
979 1208.
- 980 Zanna, L., P. P. Mana, J. Anstey, T. David, and T. Bolton (2017), Scale-aware de-
981 terministic and stochastic parametrizations of eddy-mean flow interaction, *Ocean*
982 *Modelling*, *111*, 66–80.